Journal of Volcanology and Geothermal Research 387 (2019) 106652

Contents lists available at ScienceDirect

Journal of Volcanology and Geothermal Research

journal homepage: www.elsevier.com/locate/jvolgeores

Landscape evolution associated with the 2014–2015 Holuhraun eruption in Iceland

L.E. Bonnefoy [a,b,*], C.W. Hamilton [c], S.P. Scheidt [d], S. Duhamel [e], Á. Höskuldsson [f], I. Jónsdottir [f], T. Thordarson [f], U. Münzer [g]

[a] Laboratoire d'Etudes Spatiales et d'Instrumentation en Astrophysique (LESIA), Observatoire de Paris-Meudon, LESIA (Bât. 18), 5, place Jules Janssen, 92195 Meudon Cedex, France
[b] Laboratoire Atmosphères, Milieux, Observations Spatiales (LATMOS), UVSQ/CNRS/Paris VI, UMR 8190, 78280 Guyancourt, France
[c] Lunar and Planetary Laboratory, University of Arizona, 1629 E. University Blvd., Tucson, AZ 85721, USA
[d] Planetary Science Institute, 1700 East Fort Lowell, Suite 106, Tucson, AZ 85719, USA
[e] Lamont-Doherty Earth Observatory, Division of Biology and Paleo Environment, P.O. Box 1000, 61 Route 9W, Palisades, NY 10964, USA
[f] Faculty of Earth Sciences, University of Iceland, Sturlugarta 7, 101 Reykjavík, Iceland
[g] Ludwig-Maximilians-University Munich, Department of Earth and Environmental Sciences, Section Geology, Luisenstr. 37, 80333 Munich, Germany

ARTICLE INFO

Article history:
Received 1 March 2019
Received in revised form 26 July 2019
Accepted 27 July 2019
Available online 1 August 2019

ABSTRACT

The 2014–2015 Holuhraun eruption in Iceland developed between the outlet glacier Dyngjujökull and the Askja central volcano and extruded a bulk lava volume of over 1 km^3 onto the floodplain of the Jökulsá á Fjöllum river, making it the largest effusive eruption in Iceland during the past 230 years. Time-series monitoring using a combination of traditional aerial imaging, unmanned aerial systems, and field-based geodetic surveys, established an unprecedented record of the hydrological response of the river system to this lava flow. We observed: (1) the formation of lava-dammed lakes and channels produced during dam-breaching events; (2) percolation of glacial meltwater into the porous and permeable lava, forming an ephemeral hydrothermal system that included hot pools and hot springs that emerged from the lava flow front; and (3) the formation of new seepage channels caused by upwelling of water around the periphery of the lava flow. The observations show that lava flows, like the one produced by the 2014–2015 Holuhraun eruption, can cause significant hydrological changes that continue for several years after the lava is emplaced. Documenting these processes is therefore crucial for our interpretation of volcanic landscapes and processes of lava–water interaction on both Earth and Mars.

1. Introduction

Effusive volcanic activity is one of the dominant processes shaping the surface of the Earth and other planetary bodies (Self et al., 1998). Eruptions generating ≥1 km^3 Dense Rock Equivalent (DRE) of lava only occur in Iceland every few hundred years (Thordarson and Höskuldsson, 2008). The infrequency of these events makes it difficult to fully understand their consequences in terms of landscape evolution. The 2014–2015 Holuhraun eruption provides us with the first opportunity to directly monitor processes of landscape evolution associated with a basaltic lava flow of this magnitude in an analog environment for sandsheets on the surface of Mars (Dundas et al., 2017; Sara, 2017; Sara et al., 2017).

After a brief precursor event on August 29, 2014, the main phase of the effusive eruption began on August 31, 2014 and lasted until February 27, 2015, covering an area of 83.53 km^2 (Pedersen et al., 2017; Voigt et al., 2017; Voigt and Hamilton, 2018). There are several estimates of the bulk lava volume emplaced during this ~6-month period, ranging from 1.44 ± 0.07 km^3 to 1.8 ± 0.2 km^3 (e.g., Gudmundsson et al., 2016; Höskuldsson et al., 2016; Jaenicke et al., 2016; Münzer et al., 2016; Dirscherl and Rossi, 2017; Bonny et al., 2018). Converted to DRE, volume estimates range from 1.21 km^3 (Bonny et al., 2018) to 1.36 ± 0.07 km^3 (Dirscherl and Rossi, 2018), but these DRE values may have been overestimated because they do not take into account macroscale porosity between the lava blocks forming the crustal carapace of the flow. This makes the 2014–2015 eruption at Holuhraun the largest outpouring of lava in Iceland since the 1783–1784 Laki eruption (14.7 km^3 DRE; Thordarson and Self, 1993). The lava partially covers the Dyngjusandur outwash plain where the river Jökulsá á Fjöllum originates (Arnalds et al., 2016; Pedersen et al., 2017) as well as two older Holuhraun lava flows erupted in 1792 and 1867 and Askja lava flows erupted in 1924–1929 (Hartley and Thordarson, 2013; Hartley et al., 2016). The eruption was preceded by a laterally propagating earthquake swarm (Sigmundsson et al., 2015; Gudmundsson et al., 2016) and three small subglacial eruptions

* Corresponding author at: Laboratoire d'Etudes Spatiales et d'Instrumentation en Astrophysique (LESIA), Observatoire de Paris-Meudon, LESIA (Bât. 18), 5, place Jules Janssen, 92195 Meudon Cedex, France.
E-mail address: Lb543@corneLL.edu (L.E. Bonnefoy).

https://doi.org/10.1016/j.jvolgeores.2019.07.019
0377-0273/

(Reynolds et al., 2017). It was also accompanied by graben subsidence (Hjartardóttir et al., 2016; Ruch et al., 2016), sulfur outgassing (Gíslason et al., 2015; Ilyinskaya et al., 2017), and simultaneous subsidence in the Barðarbunga caldera (Gudmundsson et al., 2016; Rossi et al., 2016; Dirscherl and Rossi, 2017).

The time-series dataset presented in this study reveals both catastrophic and continuous hydrological changes in the vicinity of the 2014–2015 Holuhraun lava flow. Observations of these events are important for understanding lava-induced changes in hydrologic activity on Earth and for interpreting those preserved within the geological record of Mars. For instance, lava–induced hydrothermal systems have the potential to generate habitable environments for extremophile life (Baratoux et al., 2011; Cousins et al., 2013) and observation of groundwater seepage near a lava flow may provide some insight into the possibility of Martian seepage channels (Baker et al., 1990, 2015; Goldspiel and Squyres, 2000). Additionally, the implications for geological hazard mitigation, especially relating to the formation and breaching of lava-dammed lakes could have significant impacts in populated areas.

In this study, we provide an overview of the 2014–2015 Holuhraun eruption, as well as the processes leading to the formation of theater-headed channels by seepage erosion. We then summarize the characteristics of aerial images and topography obtained before the eruption (summers of 2003 and of 2013) and during the summers of 2015, 2016, 2017, and 2018. These remote sensing data are combined with yearly field measurements of key water characteristics and with daily summer eyewitness observations of the area of interest by the authors or the Vatnajökull National Park rangers. Landscape evolution processes observed include the development and modification of hot springs emerging from the lava, the development of seepage channels near the lava flow margin, and changes in the structure of river channels from year to year linked to the formation and collapse of a lava-dammed lake in 2016. Comparing the changes brought about by catastrophic processes (i.e., dam-breaching events) and continuous processes (e.g., seepage erosion) suggests that the two have different, but comparably important effects on landscape evolution after the deposition of a lava flow. This result, beyond being applicable to our understanding of fluvio-volcanic processes on Earth, also has implications for Mars, where both floods and groundwater seepage may have been major agents of surface change, especially as linked to volcanic events.

2. Background

2.1. Influences of basaltic lava flow emplacement on hydrology

Lava flows tend to occupy topographic lows, and often encounter river drainage systems. Lava-dammed lakes associated with low viscosity basaltic lavas are found throughout the world (e.g., Lowe and Green, 1987; Huscroft et al., 2004; Roach et al., 2008; Allen et al., 2011; Ely et al., 2012). For example, the 1719–1721 eruption at Wudalianchi, China formed five lava-dammed lakes (Feng and Whitford-Stark, 1986). However, if the topography permits it, the river may instead change its course, often by following the boundary of the lava flow-field, as in the case of 1783–1784 Laki lava flow-field (Thordarson and Self, 1993; Thordarson et al., 2003), the Snake River in Idaho (Stearns, 1936), and the McKenzie River in Oregon (Deligne, 2012).

Basaltic lava flows also affect groundwater systems. Solidified basalt lava has a high porosity and permeability, due to the presence of vesicles, cooling-contraction joints, and lava tubes. Subaerial basaltic lava flows therefore tend to transport surface water into aquifers, leading to very little surface runoff as streams and lakes disappear into the basalt (Stearns, 1942). Lava-dammed lakes often use the lava itself as an outlet, as in Clear Lake, Oregon (Deligne, 2012). The aquifers developed in basalt can be extensive and lead to the formation of springs along their margins, as has been observed for example in the Snake River Plain in Idaho (Stearns, 1936) as well as in young lava flows in Iceland and Australia (Kiernan et al., 2003). However, the permeability of basalt decreases with time, causing groundwater flow to eventually be replaced by surface flow (Stearns, 1942; Jefferson et al., 2010). This is particularly true for lava in proglacial sandsheets (i.e., the equivalent of sandur plains in Iceland), where regular flooding transports fine material into the lava, thus filling pores and decreasing its permeability. The 2014–2015 Holuhraun lava flow-field provides the first opportunity to monitor how the groundwater system reacts to a large lava flow.

2.2. Local geological context

Our study area extends from the Dyngjujökull outlet glacier of Vatnajökull to Askja, and encompasses the region covered by the 2014–2015 Holuhraun lava flow-field (Fig. 1). The new flow-field overlies a proglacial sandsheet (Mountney and Russell, 2004), which typically is covered in snow from September/October to May/June, and then partially flooded on a diurnal basis during the summer by glacial meltwater (Bahr, 1997; Maizels, 2002; Arnalds et al., 2016). The glacial outwash sediment, deposited by episodic flooding and possibly also by glacial outburst floods ("jökulhlaups" in Icelandic), provides source material to the Dyngjusandur sandsheet (Mountney and Russell, 2004; Alho et al., 2005; Baratoux et al., 2011; Sara, 2017; Baldursson et al., 2018). Tributaries to the Jökulsá á Fjöllum that flood the outwash plain are banked on the north side by older lava flows erupted from the Askja volcanic system in the north, from the Bárðarbunga–Veiðivötn system in the west and from the Kverkfjöll system in the east; the youngest of these are mapped in Fig. 2. The northern part of the sandsheet thus includes a succession of lava flows from the Askja volcano, the youngest of which was formed between 1924 and 1929 (Hartley et al., 2016). The three Holuhraun lava flow-fields are located in the southern part of the sandsheet (i.e., closer to the Vatnajökull ice cap) and include the flow-fields formed in 1797 and 1867. These two flow-fields originated from separate 1 to 2–km–long fissure segments that trend just east of north and are situated close to the southern terminus of Askja fissure swarm (Hartley and Thordarson, 2013). The 2014–2015 eruption reactivated the 1867 fissure segment, generating new vents superimposed on the 1867 vents, erupting lava onto Dyngjusandur and covering part of the Jökulsá á Fjöllum riverbed (e.g., Ruch et al., 2016; Pedersen et al., 2017; Eibl et al., 2017; Fig. 2).

The dominant hydrological features within the region of interest include outlet glaciers from Vatnajökull, the Jökulsá á Fjöllum and the surrounding floodplain (i.e., Dyngjusandur), a lake (Dyngjuvatn), and numerous seepage channels. Lake Dyngjuvatn, located between Askja and the small interglacial shield volcano Vaðalda, is fed mainly by seasonal melt from Askja and has no outlet (Graettinger et al., 2013). Instead, water either drains into the ground or evaporates throughout the summer, leaving it mostly dry by the time snowfall begins again. At the Upptyppingar gauging station in the Jökulsá á Fjöllum (Fig. 1), 98.1% of the river discharge comes from a combination of springs and glacial melt (Esther Hlíðar Jensen, personal communication, 2018). This indicates that runoff from precipitation is a negligible source of water in the Holuhraun lava field. The glacial water contributing to the Jökulsá á Fjöllum discharge at Upptyppingar comes from the Dyngjujökull and Kverkfjöll outlet glaciers. Most of the water flowing across Dyngjusandur and around and through the 2014–2015 Holuhraun lava is from Dyngjujökull, while the streams from Kverkfjöll take a slightly more eastern course. The springwater contribution to the Jökulsá á Fjöllum includes a large seepage channel called Svartá, which is fed by a shallow aquifer system. The Svartá seepage channel emerges to the northeast of the 2014–2015 Holuhraun lava flow-field and forms a small stream system that runs along the edge of the Vaðalda shield volcano for about 900 m before reaching the Jökulsá á Fjöllum (Fig. 1).

Prior to the 2014–2015 eruption, the braided streams covering much of Dyngjusandur over the summers supplied water into the Jökulsá á Fjöllum. Small seepage channels were also common near the banks of the Jökulsá á Fjöllum about 20 km downstream from the Dyngjujökull glacier (e.g., Fig. 6a). During the winter, springs with a nearly constant

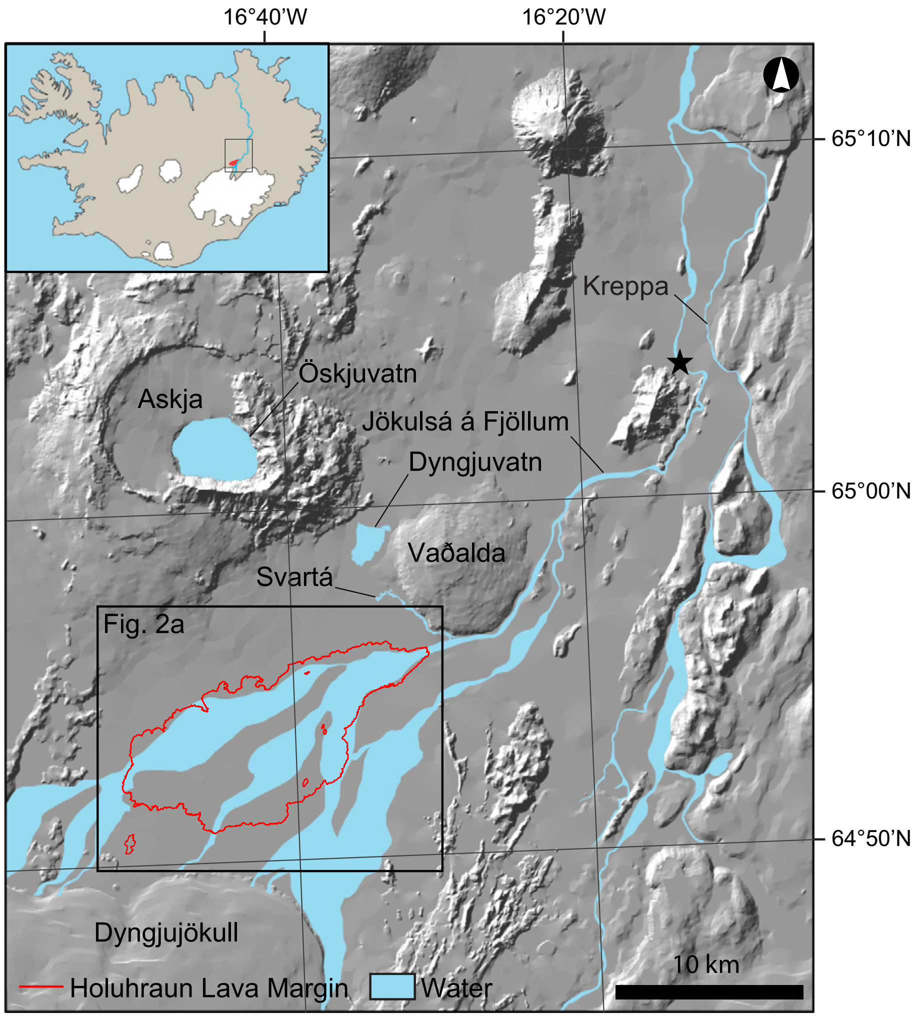

Fig. 1. The region of interest, located north of the Vatnajökull ice cap. Main landmarks are named and the pre-eruption drainage patterns on Dyngjusandur are illustrated schematically. Also shown is the outline of the 2014–2015 Holuhraun lava flow-field. Features were mapped at a digitizing scale of 1:25000. The background image is the IS50 hillshade from the National Land Survey of Iceland. The location of the Upptyppingar gauging station is indicated with a star. Inset shows the location of the figure within Iceland.

discharge of about 20 m^3/s, similar to that of Svartá, emerged within the riverbed (Baldursson et al., 2018). Thus, where Svartá merges with the Jökulsá á Fjöllum at the foot of Vaðalda, both streams had comparable winter fluxes of about 20 m^3/s. After this point, the river is fed by more small springs in winter and glacial meltwater in summer. The winter (October to April) discharge measured at Upptyppingar was usually

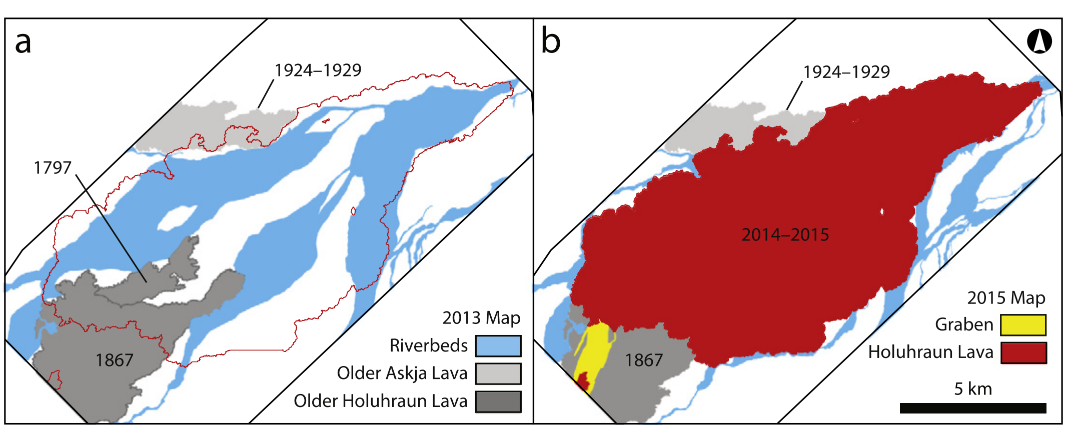

Fig. 2. (a) Map of the pre-eruption landscape, showing the active riverbeds and lava flows <300 years old. The 2014–2015 Holuhraun lava flow-field is outlined in red. (b) Map of the post-eruption landscape (2015). Features were mapped at a digitizing scale of 1:2000.

55–60 m^3/s, whereas the average August discharge measured between 1972 and 2015 was around 200 m^3/s (Gylfadóttir, 2016). Thus during the winter, springwater provides the main contribution to the Jökulsá á Fjöllum at Upptyppingar; while during summer, most of the water is supplied by glacial melt.

The regional topographic slope and orientation of the Askja fissure swarm likely exert strong controls on the groundwater flow directions in the vicinity of the 2014–2015 Holuhraun lava flow-field (Baldursson et al., 2018). However, to the north groundwater flow patterns may be complicated by surface runoff and seasonal meltwater contributions from the Askja massif and Vaðalda lava shield.

2.3. The 2014–2015 Holuhraun eruption

The 2014–2015 Holuhraun eruption was preceded by an intense earthquake swarm that was detected along the SE margins of the 10-km-diameter Bárðarbunga caldera on August 16, 2014. The propagation of this seismic swarm has been interpreted as the movement of magma through a dike 45 km toward the northeast (Sigmundsson et al., 2015). When the magma reached the surface in Dyngjusandur, about 7 km north of the Dyngjujökull outlet glacier of Vatnajökull, it became a fissure eruption. The first phase of the eruption lasted 4 h on August 29, 2014 (Sigmundsson et al., 2015). It is possible that several small eruptions took place underneath the Vatnajökull glacier, as indicated by the development of "ice cauldrons", which are circular depressions formed in ice surface by melting of the base of the ice (e.g., Reynolds et al., 2017). The main phase of the eruption lasted from August 31, 2014 to February 27, 2015, producing a lava flow-field covering an area of approximately 83.53 km^2. A visible graben with vertical displacement up to 5 m formed around the erupting vents during the early stages (the first three days) of the eruption (Hjartardóttir et al., 2016; Ruch et al., 2016). Though the eruption generated considerable sulfur outgassing, its environmental impact was largely mitigated by the weak eruption intensity, the low (typically <4 km) eruption plumes, and the remoteness of the area in the sparsely vegetated highlands (e.g., Gíslason et al., 2015). During this time a gradual subsidence was observed of the Bárðarbunga caldera (e.g., Gudmundsson et al., 2016; Dirscherl and Rossi, 2017).

A unique aspect of the eruption was that its lava flows encountered the Jökulsá á Fjöllum, Iceland's highest discharge river, on September 7, 2014, and then proceeded to cover part of the riverbed, causing a reorganization of the fluvial system within the region. The landscape before and after the eruption is shown in Fig. 2. Initially, the lava was bounded by the riverbanks and the Askja 1924–1929 lava flow-field, but subsequent breakouts covered these boundaries (Pedersen et al., 2017; Kolzenburg et al., 2018). While explosive water–lava interactions were observed on September 8, 2014, no explosive constructs were formed (Pedersen et al., 2017). At the distal (east) end of the lava flow-field, lava-induced hydrothermal activity formed hot springs, which were still warm (10.7 °C) in the summer of 2018. Herein, we refer to this locality as the "hot springs region" (Fig. 3). The deposition of lava within the riverbed also led to the development of two lava-dammed lakes, which we refer here to as the "western lake" and "eastern lake" (Fig. 3). The streams feeding the lava-dammed lakes originate from different parts of the glacier and are separated by the older Holuhraun lava flow-fields. These two streams were already separate before the 2014–2015 eruption (e.g., Figs. 1 and 2). In 2016, the eastern lake breached through to the hot springs region; this event is described in detail in Section 4.3. After July 22, 2016, glacial stream water and water from the hot springs merged to produce braided network streams with a wide range of temperatures.

2.4. Seepage channels

In the region of interest, the Jökulsá á Fjöllum is fed not only by glacial melt, but also by seepage springs, such as Svartá (Fig. 4), which is an archetypal example of a seepage channel formed within unconsolidated sediment (Woodruff and Gergel, 1969; Higgins, 1982). Non-artesian springs form when the groundwater table intersects with the surface, leading to the formation of a stream. In unconsolidated sediment, as within Dyngjusandur, groundwater sapping erodes the base of the channel, creating an overhang and eventually leading to a collapse of the headwall. The term "sapping" designates the erosion of the base of a scarp causing the creation of an overhang (Dunne, 1990; Lamb et al., 2006; Pelletier and Baker, 2011). The collapsed sediment is then evacuated by the flowing stream (Schorghofer et al., 2004). Seepage channels therefore grow by headward erosion and form characteristic theater-shaped heads (Fig. 4; Higgins, 1982; Dunne, 1990). As the individual channels grow, groundwater flow converges to the channel head, increasing headward erosion (Dunne, 1980; Baker et al., 1990). The Svartá theater-shaped channel heads are up to 10 m high and are formed of steep slip faces of sand (Mountney and Russell, 2004). Mountney and Russell (2004) report seeing 1–2-m-wide slabs of sand sliding down the slip face due to sapping eroding its base. They also report the presence of a pebbly gravel layer at the base of the slip faces and it is likely that much of the groundwater flow occurs within this gravel layer.

3. Methodology

3.1. Aerial data

To monitor the hydrology of the region, we compare high-resolution imagery and topography from different sources at five time periods, one before the eruption (2003/2013) and four after the eruption, during the summers of 2015, 2016, 2017, and 2018. In each case, observations were collected in the summer months using traditional aircraft and small unmanned aerial systems (sUAS). The highest resolution datasets are obtained during our field campaigns in 2015, 2016, 2017, and 2018 using sUAS. These data include 5–20 cm/pixel stereo-derived digital terrain models (DTMs) and 1–4 cm/pixel orthomosaics covering 21% of the flow, including repeat imagery of several regions in 2015, 2016, 2017, and 2018 (Voigt et al., 2017; Voigt and Hamilton, 2018). To investigate hydrological changes associated with the Holuhraun lava flow-field, we focus on a subset of these data, obtained at the distal northern end of the field where hot springs emerge from a flow front (Fig. 3). The datasets used in this study are described further in Table A1 and in Sections 3.1.1–3.1.3; the location of subsequent figures is given in Fig. 5. The 2015–2018 sUAS datasets are freely available via the University of Arizona Spatial Data Explorer Geoportal (Scheidt and Hamilton, 2019).

3.1.1. Pre-emplacement datasets (2003–2014)

The pre-emplacement DTM and orthomosaic were acquired and processed by Loftmyndir ehf. from airborne photogrammetry datasets taken on August 12, 2013 over most of the region and on August 23, 2003 in the hot springs region. The DTM was generated by combining datasets and smoothing the seams. The spatial resolution of the DTM is 5 m/pixel, and estimated 1 sigma error bars in elevation vary from $\pm$0.5 m to $\pm$5 m (Appendix A). The orthoimage has a spatial resolution of 50 cm/pixel. The Environmental Systems Research Institute (Esri) ArcGIS World imagery basemap, which is a combination of multiple datasets (sources: Esri, DigitalGlobe, GeoEye, i-cubed, USDA FSA, USGS, AEXm Getmapping, Aerogrid, IGN, IGP, Swisstopo, and the GIS user community), was also used to provide regional context.

3.1.2. The 2015 dataset

The 2015 regional DTM (Appendix A, Fig. A1) uses a combination of datasets to obtain the best possible quality of data over the whole region. LiDAR data, collected and processed by the Natural Environment Research Council (NERC) was acquired on September 4, 2015, and had at this time the highest spatial (2 m/pixel) and vertical (mean error of 4 to 5 cm depending on the flight line) resolution over the majority of

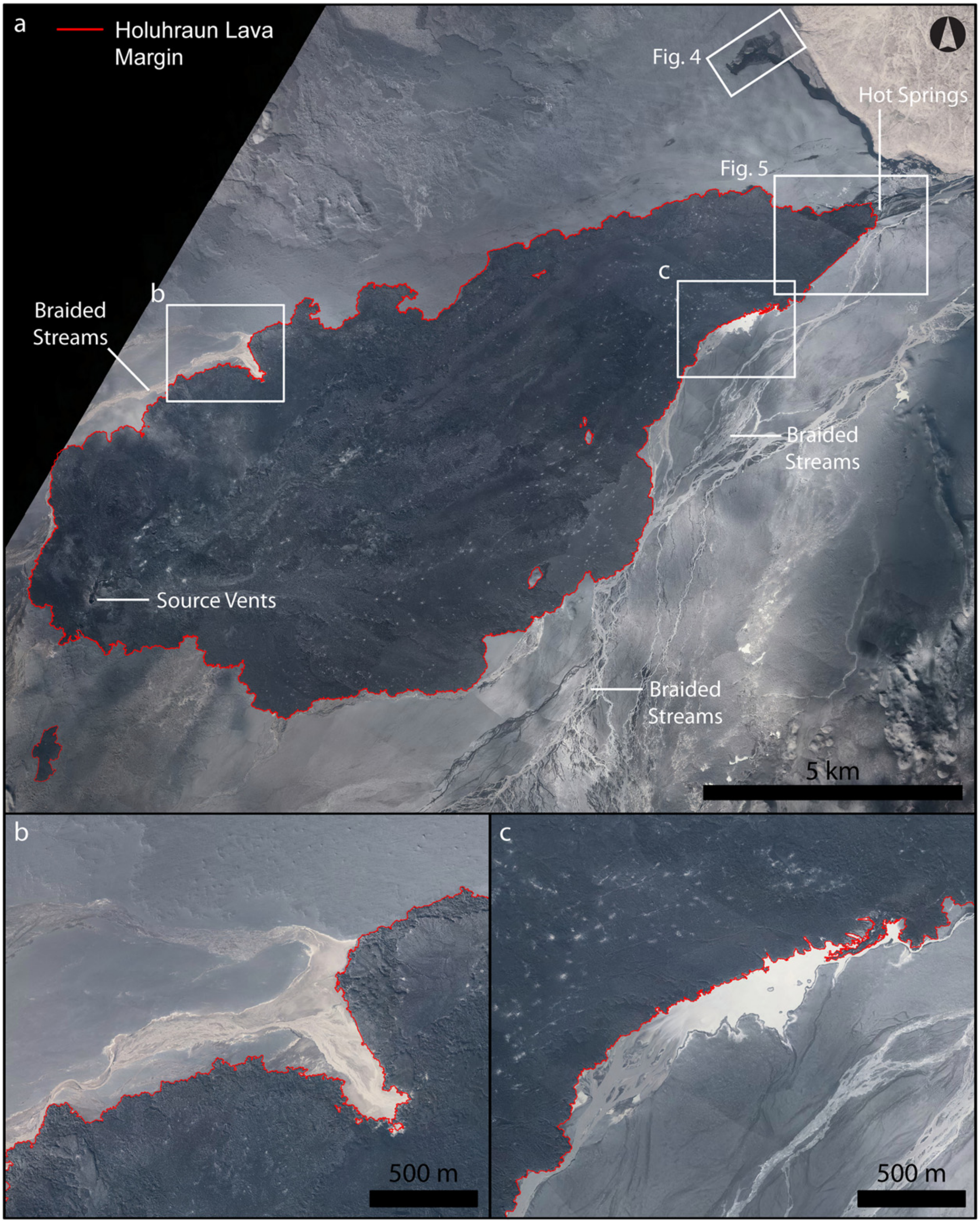

Fig. 3. (a) Detail of the lava flow and its surroundings in 2015, showing the location of two proceeding figures. The lava flow-field margins are shown in red. The background image is a 20 cm/pixel UltraCam-Xp true orthophotomosaic acquired on September 8, 2015 (IsViews, LMU Munich). The two different lava-dammed lakes are shown in (b) and (c). (b) Detail of the lava-dammed lake on the northwestern margin of the flow. This lake has changed little from 2016 to 2018. (c) Detail of the lava-dammed lake on the eastern margin of the flow-field. This lake breached in July 2016; the stream now follows the margin of the lava into the hot springs region. The pale spots on the lava have been identified as thernadite, a sulfate, and indicate the position of fumerolic activity (Aufaristama et al., 2019).

the lava flow. Eight flights lines were made over the Holuhraun lava flow-field: seven of these are parallel and aligned with the long axis of the field (from the vent to the hot springs region) while the eighth is transverse and crosses all the others. The LiDAR therefore does not cover the entirety of the flow-field. Furthermore, small clouds and fumeroles obscured parts of the lava, and created gaps in the data. Where LiDAR data was unavailable, we used another photogrammetry-derived DTM provided by Loftmyndir ehf. using data taken on August 30, 2015. Where clouds obscured interior parts of the 2014–2015 Holuhraun flow-field, occluded regions were masked and

Fig. 4. Source region for the Svartá seepage channel, showing its appearance in (a) August 2014 (source: DigitalGlobe) and (b) September 2015 (UltraCam-Xp true orthophotomosaic, IsViews, LMU Munich). The height of headwalls in this region is approximately 6–8 m in height. The dark color of the sand surrounding Svartá is caused by water saturation, implying a shallow aquifer.

interpolated using Loftmyndir ehf. data. Where clouds covered the edge of the flow, contour lines were interpolated using Esri ArcGIS editing tools for every meter using the orthoimage as reference. The post-emplacement imagery includes the 50 cm/pixel August 30, 2015 orthoimage provided by Loftmyndir ehf., as well as a 20 cm/pixel true orthophotomosaic derived from UltraCam-Xp airborne data (captured on September 8, 2015) and provided through the IsViews project (Ludwig-Maximilians-University of Munich). During the 2015 field campaign, sUAS image observations were also made in selected regions using two DJI Phantom 3 Pro quadcopters, each equipped with a 12 MP image camera. With a flight altitude of 100 m, a ground sampling distance (GSD) of 4 cm/pixel is achieved. Image data were imported into the software package Pix4Dmapper Pro to produce orthoimages and DTMs. A DTM produced from image data with a 4 cm GSD has a spatial resolution of 16 cm/pixel. Ground control points (GCPs) were placed in the field and surveyed using a Trimble R10 differential global positioning system (DGPS). Although the sUAS has GPS for navigation, its accuracy and precision is low. The R10 DGPS is capable of producing survey points with excellent precision (0.8 cm horizontal and 1.5 cm vertical); therefore, these survey points were used in Pix4Dmapper Pro to accurately georeference orthoimages and DTMs. In addition to GCPs, Phantom sUAS surveys were co-registered to high spatial resolution data products (2016 orthoimages and DTMs) produced by differentially corrected UX5-HP surveys (described below in Section 3.1.3).

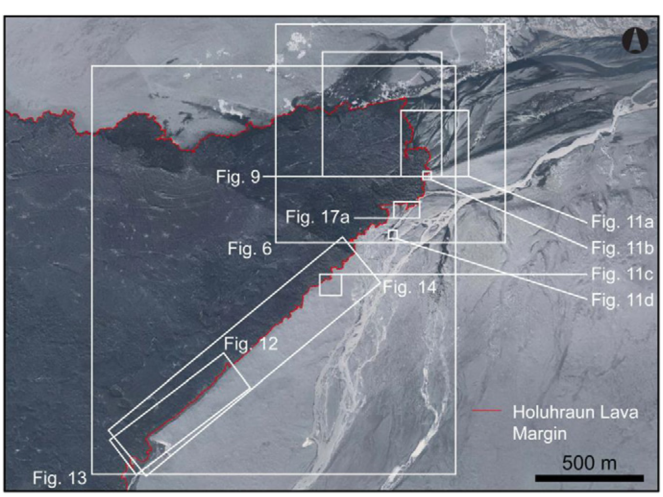

Fig. 5. The distal end of the lava flow, showing the location of proceeding figures. The lava flow margin is shown in red. The background image is a 20 cm/pixel UltraCam-Xp true orthophotomosaic acquired on September 6, 2015 (IsViews, LMU Munich).

3.1.3. The 2016, 2017, and 2018 datasets

During our field campaigns in August of 2016, 2017, and 2018, sUAS data were obtained over the 2014–2015 Holuhraun lava flow-field. All 2016 and 2018 image data were acquired using a Trimble UX5-HP fixed-wing unmanned aircraft (Cosyn and Miller, 2013; Pauly, 2016). This sUAS has a dedicated GPS for autonomous navigation as well as a separate DGPS receiver for recording a raw GPS data stream. During UX5-HP flights, a base station continuously records raw GPS data as well. In post-processing in Trimble Business Center, the base station and fixed-wing GPS data are used to calculate the positions of the plane at the exact instances of image acquisition from a Sony a7R camera. Images are 36 MP and capture exceptional detail of the ground surface. Because each image is accurately georeferenced and combined with camera pointing information using the UX5-HP's inertial measurement unit (IMU), GCPs are not needed to complete an accurate and precise stereophotogrammetric survey. Image data in 2017 were taken using a DJI Phantom 4 Pro quadcopter and was processed into DTMs and orthoimages using Pix4Dmapper Pro These data were co-registered to common ground targets and features seen in the 2016 UX5-HP orthoimage and DTM. The 2016 and 2017 data is concentrated on the hot springs region and the eastern lava-dammed lake.

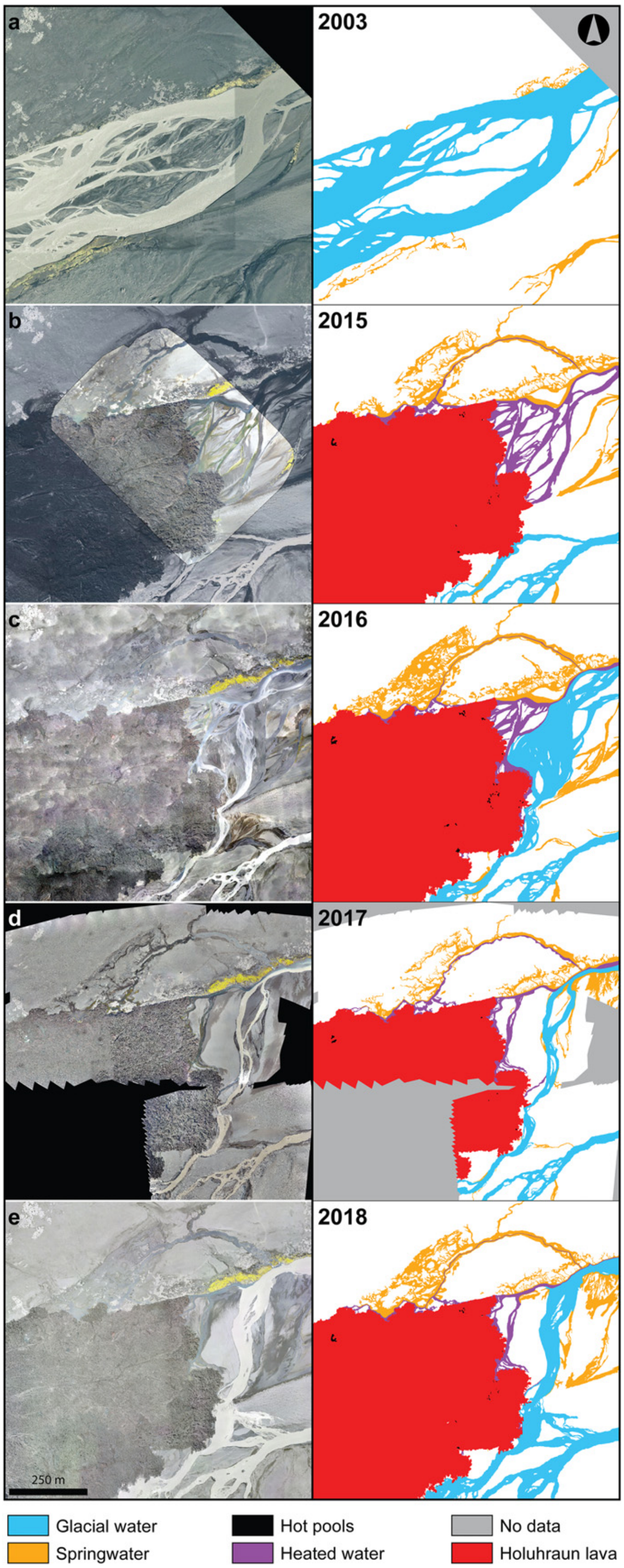

Fig. 6. Evolution of the hot springs region. Maps shown in the right column identify the locations of glacial water, springwater, hot pools, and heated water as well as the 2014–2015 Holuhraun lava flow. These different water sources were inferred from temperature measurements as well as water flow directions; when several different sources merge, all colors are used in the channel. Note the development of seepage channels to the North, as well as the breakthrough of the glacial water into the hot springs region in 2016. Note also that every year, a small amount of heated water flows northward, but the cold seepage water dominates the temperature in these streams. Features were mapped at a scale of 1:300. (a) 50 cm/pixel orthoimagery from Loftmyndir ehf. showing the landscape configuration in 2013. (b) 2015, 4 cm/pixel orthoimagery acquired using a DJI Phantom 3 Pro sUAS, superimposed on 20 cm/pixel UltraCam-Xp true orthophotomosaic (IsViews, LMU Munich). (c) 2016, 4 cm/pixel orthoimagery acquired using a Trimble UX5-HP sUAS. (d) 2017, 2 cm/pixel orthoimagery acquired using a DJI Phantom 4 Pro sUAS. (e) 2018, 4 cm/pixel orthoimagery acquired using a Trimble UX5-HP sUAS.

3.2. Mapping

Maps were constructed at three scales and include: (1) a context map depicting the pre-eruption hydrology (Fig. 1); (2) two regional maps focused on the landscape directly around the 2014–2015 Holuhraun lava flow-field (Fig. 2), and (3) five detailed maps of the hot springs region illustrating annual changes (Fig. 6). All mapping was completed using ArcGIS software by Esri.

The pre-eruption hydrological context map (Fig. 1) shows surface water features and the lava flow outline. This map covers 2190 km^2 and was digitized at a scale of 1:25000 using the pre-emplacement Loftmyndir ehf. orthomosaics and ArcMap basemap images.

The regional maps (Fig. 2) show the 2014–2015 Holuhraun lava flow-field and its immediate surroundings, both before (in 2003 and 2013) and after (in 2015) the eruption. Here, we also show the 2014–2015 Holuhraun lava flow-field outline, and to establish geological context, we included other lava flow-fields in the region with ages <300 years as well as riverbeds that were active in 2003/2013 and 2015. However, the position of the Jökulsá á Fjöllum tributaries flowing through the flood plain varies daily over the summer. These streams are often only centimeters to tens of centimeters deep and, as they flow over the highly permeable ground, they are often absorbed before they reach the main riverbed. We therefore rely primarily on the topographic boundaries to map the extent of channels hosting the braided stream system. The two maps in Fig. 2 each cover 165 km^2 and were digitized at a scale of 1:2000 using the pre-emplacement and 2015 datasets described above.

Maps of the hot springs region (Fig. 6) were developed for 2003, 2015, 2016, 2017, and 2018. These maps focus on the different sources of water, which were identified with the following definitions, using stream color, morphology, temperature, and flow directions. "Heated water" corresponds to warm (>8 °C) water, which emerges from the lava and has a blue or green color due to the presence of sulfates and algae. "Glacial water" can be traced back to the Dyngjujökull outlet glacier on the northern part of Vatnajökull ice cap. While rain and groundwater contribute to these streams, the main source of the water is glacial melt from the glacier. "Glacial water" has high turbidity and is milky white in color due to the entrainment of fine particles. "Spring water" streams are identified by being sourced directly out of the ground, and are clear water, filtered by the sand and rock. "Spring water" channel heads often have the theater-headed morphology characteristic of seepage channels (see Fig. 4). Where two different types of water meet in one stream, we use both colors, with the width of each color approximately representing the contribution of each water source (this can vary during the day with the glacial river water levels). Finally, we refined the lava flow outline in the hot springs region for each year to account for the rising and lowering of the surrounding water levels. Maps of the hot springs region each cover 0.94 km^2 and were digitized at 1:300-scale using the highest-resolution data available each year.

3.3. Hydrological analysis

The discharge rate and heat flux of the different streams was investigated in 2016, 2017, and 2018 using systematic stream flow measurements, such as flow velocity, temperature, pH, and cross-sectional area. In 2016, temperature and velocity data were taken on different days and at different places as the transects. We therefore used the nearest velocity and temperature measurement within the same stream for each transect. In 2017 and 2018, stream transects, velocity, pH, and temperature data were all taken at the same time. For further details, see Appendix B.

The discharge rate Q [m^3/s] is calculated for each cross-section as follows:

$$Q = v \times A, \tag{1}$$

where v is the flow velocity [m/s], and A is the cross-sectional area [m^2]. Heat flux is then calculated according to:

$$E_{flux} = C_p \times \rho \times T \times Q \tag{2}$$

where E_{flux} is the total energy flux [J/s], C_p is the specific heat of water [J/kg/K] at the water temperature, assuming $\rho = 1$ kg/m^3 is the water density, and T is the water temperature (K). The hydrology observations are given for each stream in Tables B1–B3 (Appendix B), summarized in Table 1, and discussed in Section 4.1.

To estimate the flow velocity during the July 21, 2016 dam-breaching event, we used Manning's equation:

$$v = \frac{R^{2/3} \times \theta^{1/2}}{n} \tag{3}$$

where R is the hydraulic radius [m], θ is the slope at the bottom of the stream [dimensionless], and n is the Manning coefficient [s/m$^{1/3}$]. To estimate Manning's n, we used the guide by Arcement and Schneider (1989), which is primarily based on grain size in the channel, with adjustments taking into account the vegetation (absent in our case), obstructions, and channel shape. We find $n = 0.032$, which is close to the value of 0.035 found within the Jökulsá á Fjöllum river bed by Howard et al. (2012). Under uniform flow conditions, the slope θ at the bottom of the stream is equal to the slope of the water surface. The hydraulic radius is the ratio between the cross-sectional area and the wetted perimeter. For an ideal rectangular channel, it can be calculated as follows:

$$R = \frac{W \times D}{W + 2D}, \tag{4}$$

where W is the width [m], and D the depth of the channel [m]. The hydraulic radius, and especially the depth, is the largest source of error in our calculation. Indeed, due to its location on the far side of the lava flow-field, this channel is difficult to access, and a cross-section was not obtained. Instead, for every meter along the new Jökulsá á Fjöllum riverbed, we extracted topography profiles from the 2003 DTM from Loftmyndir ehf., the 2015 Lidar data from NERC, and the 2016 DTM from the Trimble UX5-HP sUAS. For each profile we carried out measurements of the width and elevation (H_{river}) of the river in 2016, the maximum width and flood height (H_{flood}) reached by the flood as shown by high water marks (deposited or eroded material), and the pre-existing width and lowest elevation (H_{2015}) of the depression in 2015. The widths and depths we measure for the flood depend on whether the flood was eroding, depositing sediment, or running through an existing channel. The depths of the flood are calculated as $D = H_{flood} - H_{2015}$ if the flood ran through a pre-existing channel, or as $D = H_{flood} - H_{river}$ if the flood eroded an entirely new stream. However, during the breach, the morphology of the channel varied very quickly as the channel was excavated and sediment was deposited. This method therefore leads to large uncertainties in the channel depth and in the final discharge rates calculated. The results of these calculations are presented in Section 4.

3.4. Climate data

We also examined weather patterns between 2000 and 2018 to determine whether abnormal precipitation or temperature occurred in the Dyngjusandur region in this period. Given the remote location of the region, the closest weather station with publicly available data for this period is located 50 km to the north, and is not representative of the weather at Dyngjusandur. Instead, we use the climate reanalysis data available through the European Centre for Medium-Range Weather Forecasts (ECMWF) ReAnalysis-Interim (ERA-Interim) record. This worldwide dataset combines model predictions with both nearby surface and satellite observations, and gives the resulting data for every 0.125° in latitude and longitude (Dee et al., 2011). We use the monthly precipitation accumulation, and the monthly mean of the daily mean temperature, modeled for the location of the 2014–2015 Holuhraun lava flow (64.875°N, 16.500°W). These data are not direct observations obtained at the site on or near the lava flow-field, but are the results of a climate model and the nearest measurements, as given by the ERA-Interim dataset. Although we are using the ERA-Interim dataset as a proxy for weather at the Holuhraun lava flow-field, it may include inaccuracies due to both insufficient resolution and lack of ground observations.

4. Results

4.1. Yearly changes in the hot springs region

4.1.1. Morphological changes

We studied the hydrology of the hot springs region for 2003, 2015, 2016, 2017, and 2018. Fig. 7 provides visual context for some key features of this region. Here, water from three different sources meets: clear, cold spring water from seepage channels (Figs. 7c), blue–green

Table 1
Summary of the 2016, 2017, and 2018 field data in the hot springs region. For the complete data, see Appendix B. Note these data were all taken between July 25 and August 4 of their respective years. The total discharge rate and heat flux given in this table correspond only to that coming from the warm streams (including the warm half of mixed streams). The area to the North of the old Jökulsá á Fjöllum riverbed is mainly covered by seepage channels, so the last line of the table illustrates the coverage area of seepage channels. Since groundwater level regulates seepage activity, this area gives an idea of relative groundwater levels from year to year: unusually high in 2016, and low in 2017.
Dundas et al. (2017).

	2015	2016	2017	2018
Total discharge rate from under the lava (m^3/s)	–	9.3–14.0	2.2–4.3	3.0–5.2
Total heat flux from under the lava (GJ/s)	–	11.3–16.8	2.7–5.2	3.6–6.1
Stream area North of the old Jökulsá á Fjöllum riverbed in the hot springs region (m^2)	38,100	53,200	26,900	38,300

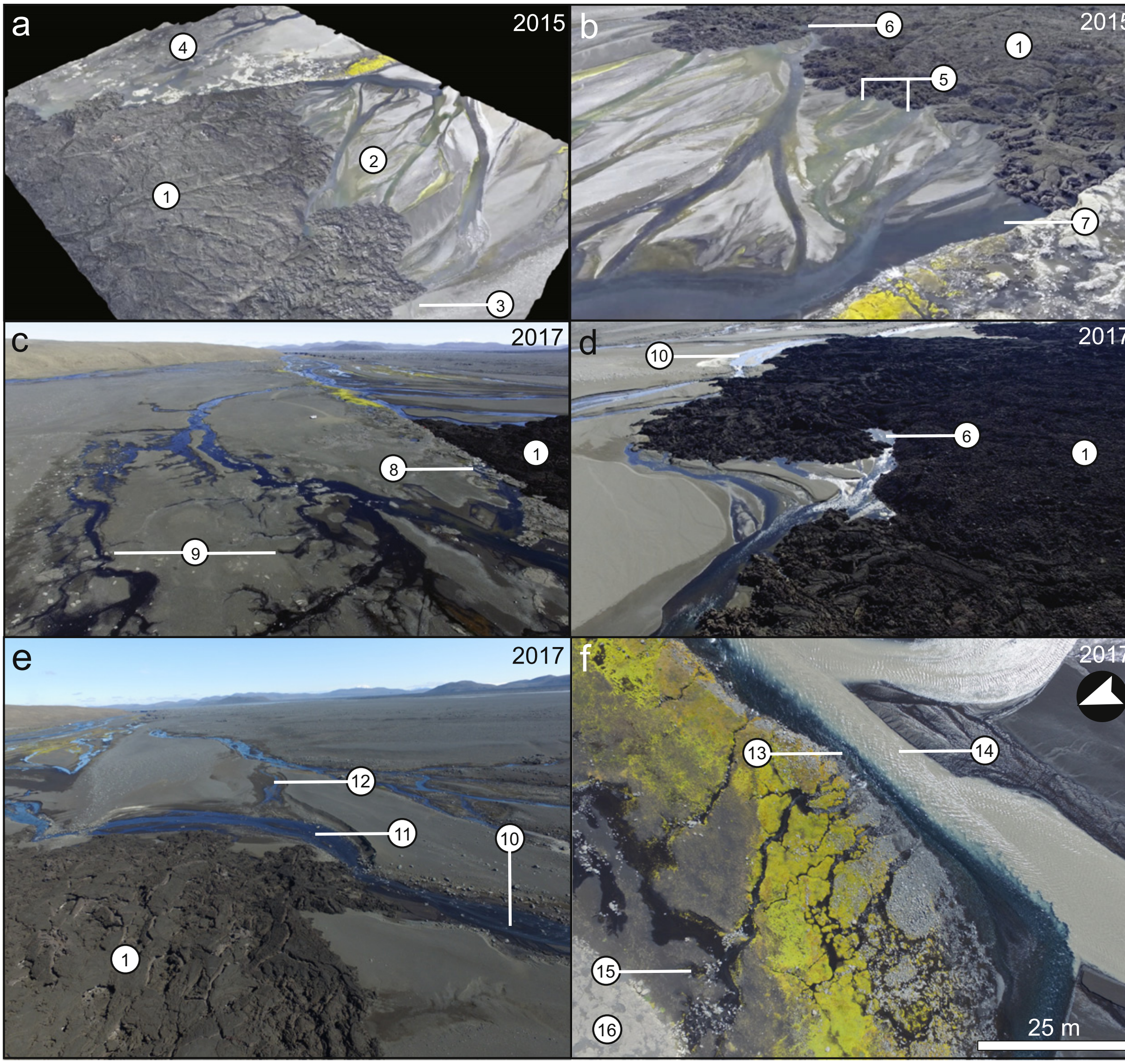

Fig. 7. (a) Perspective rending of the hot springs region in 2015, facing north. 1: Northeastern portion of the 2014–2015 Holuhraun lava flow-field. 2: Hot springs. 3: The margin of the lava abuts against the former margin of the river channel and in 2015, there were no overland flows of water at this locality. 4: Seepage channels exist in this region in 2015, and become more pronounced over the following year. (b) Perspective rending of the hot springs region in 2015, facing south. 5: In 2015, the warmest hot spring branches had the most algae and were greener. 6: Location of a warm pool. 7: Cool water dominantly fed along the margin, rather than through, the lava. (c) Perspective view of the northern margin of the lava in 2017, facing northeast. 8: Water, largely from seepage channels, flows along the margin of the lava toward the hot springs region, emerging at the location identified by 7. 9: Active seepage channels. (d) Perspective view of the northern margin of the lava in 2017, facing south. 10: Location of the stream branch formed during the 2016 dam-breaching event, which carved a new channel along the eastern margin of the lava, transporting glacial meltwater into the hot springs region. Note this is the same location as 3. (e) Perspective view of the glacial meltwater streams on the eastern side of the lava flow in 2017. 10 and 11: channel formed in 2016 feeding water toward the location of the hot springs. 12: Spillway channel connecting to another branch of the Jökulsá á Fjöllum river. When there is too little glacial melt to reach this channel, seepage is observed there. (f) Nadir-pointing view of a mixing zone north of the former hot springs region in 2017. Here, clear water (13), which is a mixture of seepage spring and lava filtered water, merges with sediment laden glacial river water (14). 15: Small seepage channels. 16: Old lava flow surfaces; these are also visible in 4.

water warmed by the lava (Fig. 7b), and milky white glacial meltwater (Fig. 7f). This mixing is particularly evident in one large stream, which remains split in two after the different streams have merged (Fig. 7f). The hot springs and hot pools, which appeared during the eruption, are still present in 2018. In 2015, an important stream of the Jökulsá á Fjöllum approached the lava but entered an eastward-flowing drainage before continuing its flow to the northeast, thereby avoiding the hot springs region (Figs. 6b and 7a). In 2016, water from the eastern lava-dammed lake reached this stream of the Jökulsá á Fjöllum drainage system, and the large water influx was sufficient to break into the hot springs (Figs. 6c, 7d, and e). The dam breaching event, which is further discussed in Section 4.3, brought glacial water into the hot springs in 2016, cooling them down and reorganizing them (Fig. 6c). The further modification of the channel morphology from 2016 to 2018 is mostly due to daily changes in water level. Even though in 2018 there is more glacial water and more seepage activity than in 2017, the morphology of the streams remains the same, indicating that the system has reached a more stable layout. The hydrological system on Dyngjusandur is thus gradually stabilizing after the large disruption by the new lava.

Before the eruption, there was already some seepage activity very close to the main bed of the Jökulsá á Fjöllum, which forms a topographic low within the sandsheet (Fig. 6a). Over the summers following the eruption, we observed the development of seepage channels around the hot springs, in particular to the north of the lava, which is covered by a much older basaltic lava flow (Fig. 6b–e; closer views in Fig. 7c and f). Indeed, the area of surface water north of the riverbed of Jökulsá á

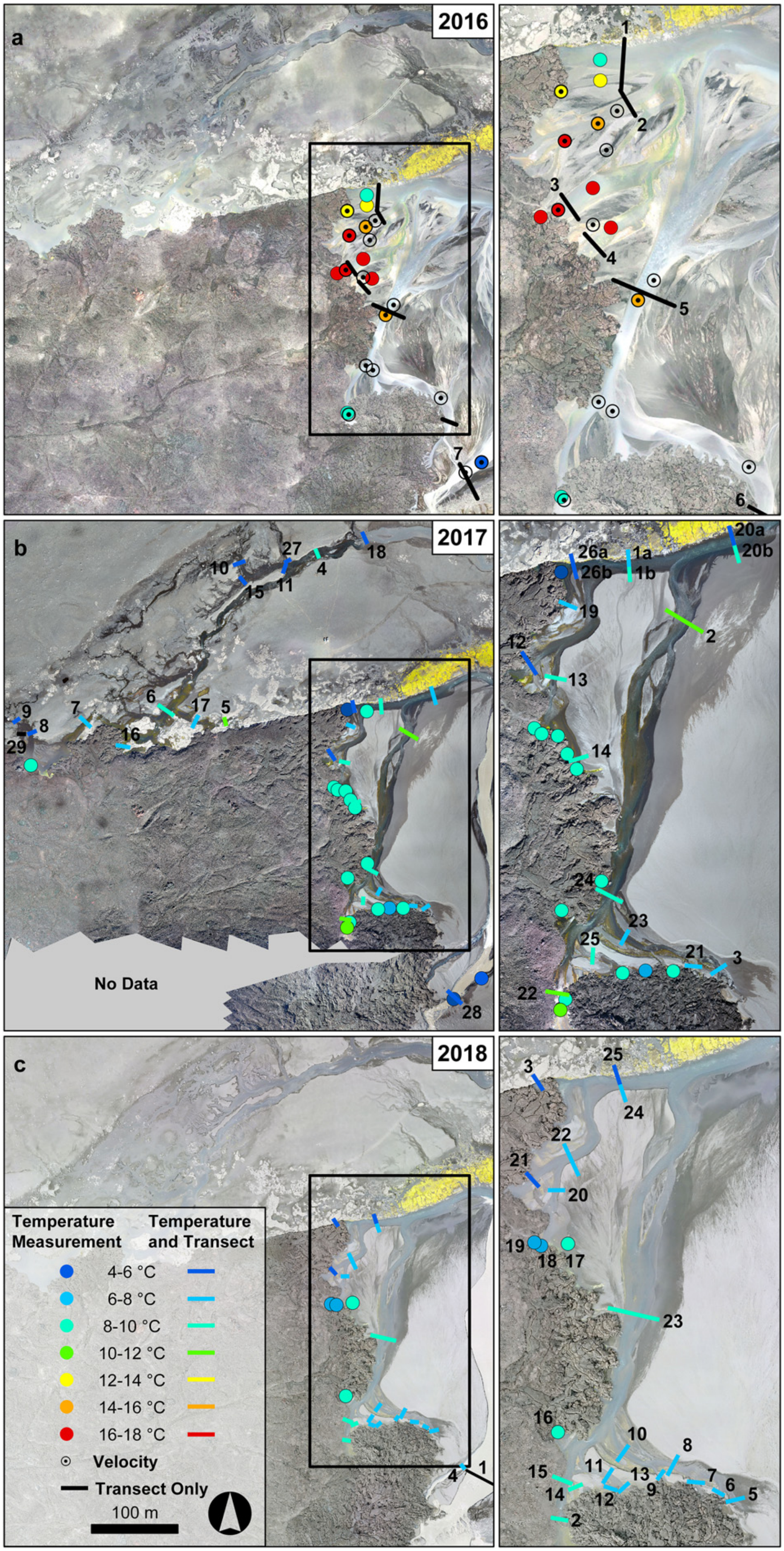
a
2016
b
2017
No Data
c
2018
Temperature Measurement
Temperature and Transect
4-6 °C
6-8 °C
8-10 °C
10-12 °C
12-14 °C
14-16 °C
16-18 °C
Velocity
Transect Only
100 m

Fjöllum (see Fig. 6) increased in size from 2500 m^2 in 2003, to 38100 m^2 in 2015, to 53200 m^2 in 2016, decreased to 26900 m^2 in 2017, and grew back to 38300 m^2 in 2018 (Table 1). Although there are some hot springs in this area, it is largely dominated by seepage channels, and the yearly changes in this area thus reflect shifting water tables. Seepage activity at Svartá seems to match the patterns observed in the hot springs region: it was high in 2016 and 2018, and lower in 2017. Given that the source of Svartá is located 2 km north of the hot springs and has an elevation that is approximately 3 m higher than the seepage channels in the hot springs region, these observations imply that seepage at Svartá and the hot springs region originates from the same shallow aquifer. The water table in this shallow aquifer rose in 2015, and was considerably higher in 2016 and 2018 than in 2015 and 2017.

In the summer of 2017, dozens of small artesian fountains were observed near the hot springs region, near profiles #9, #7, and #17 in Fig. 8b. Water associated with the artesian fountains bubbled out of the ground with heights typically <10 cm. Their fountains were generally a few centimeters wide and clustered near the heads of some seepage channels. They were only observed on a sunny day after a stretch of colder and overcast weather, and were thus correlated with a sudden rise in the water level due to increased glacial melt. It is likely that the shallow aquifer feeding the seepage channels is partly confined by the ancient lava. Thus there is a lag between the rise in water table and the rise in water level in the seepage channel. This lag is sufficient to create a small artesian head, pushing the water up tens of cm. This explains why no artesian springs were observed in 2016 or 2018 in spite of higher water levels.

4.1.2. Hot springs characteristics

The water entering the hot lava either exits down-flow to form hot springs, or it vaporizes into steam en route to form fumeroles. Due to the cooling of the lava, most fumeroles were gone by 2016, though in 2016 and 2018 levels of fumerolic activity were observed to increase on warm days when there were higher volumes of glacial runoff. We attribute enhanced fumerolic activity on warmer days to the water table reaching the level of residual heat sources within the core of the lava flow-field, thus generating steam. In 2017, when water levels in the region were lower, no major fumeroles were observed.

The water that emerged from the lava along with several nearby glacial and seepage streams were examined during the summers of 2016, 2017, and 2018 and the results are shown in Fig. 8. For each cross-section, we calculated discharge rate and heat flux through each stream (see Appendix B). These values only represent a snapshot in time for a very dynamic system: the water levels varied throughout the day and from day to day, leading to changes in discharge and heat flux. Estimates of the total discharge rate and total heat flux from the heated water going through the lava were then made by combining information from multiple stream segments, while excluding glacial water contribution (profile #7 in 2016, profile #28 in 2017, and profile #1 in 2018); they are given in Table 1.

While they do not fully illustrate the high-frequency variations over time, the 2016–2018 field observations allow us to quantify general trends in the annual distribution of temperatures, discharge rates, and heat fluxes in the hot springs region. For example, in the summer of 2016, all hot spring temperatures had decreased to below 20 °C (Fig. 8). Yet, even in 2016 Vatnajökull National Park rangers recorded high water temperatures in pools within the lava (Sigurður (Siggi) Erlingsson, personal communication, 2017), reaching up to 41 °C in the late summer (i.e., August to mid-September) of 2016. The hottest temperatures corresponded to dates when the water reached a maximum depth of 1.8 m within the pool. By late September, the water level decreased to 1.4 m within the pool and the temperature correspondingly decreased to 33 °C. This implies that in 2016, the lava contained significant residual thermal energy that was available to heat water, but only if the water table rose high enough for the water to be warmed by the hot interior of the flow. In 2017, water depths in the pool were considerably lower—just 20–30 cm at the same locality—and maximum temperatures were about 10 °C. The changing morphology of the river, caused by the dam breaching event and migration of streams, can result in varying water levels and mixtures of water of different origins. For instance, the discharge rate through the hot springs (Table 1) in 2016 is more than twice as high as in 2017 and 2018, which may be explained either by residual water from the recent dam-breaching event (a week earlier) or by extra glacial water entering the hot springs.

Changes in stream temperature and discharge rate from year to year are thus explained by three interacting processes: gradual cooling the lava flow core, changing configurations of lava-dammed lakes and stream locations, and changing water table levels.

4.1.3. Annual weather patterns

To determine whether the observed changes in water table and discharge rates were linked to the 2014–2015 Holuhraun eruption and/or to weather patterns, we examined the modeled total precipitation and mean daily temperature data described in Section 3.4, for the Holuhraun area. These datasets are shown in Tables 2 and 3 for the summers of 2003 and 2013–2018. Section 4.1.1 discussed how the groundwater level at Svartá and at the distal end of the 2014–2015 Holuhraun lava flow-field rose considerably after the eruption, and has not dropped back to its original level. Temperature and precipitation patterns within the Holuhraun region do not appear sufficiently different during the 2015–2018 time period to fully explain such a large and lasting change (Tables 2 and 3). Consequently, the local rise in groundwater level and seepage channel activity was probably affected to some degree by the lava itself.

Weather patterns might however explain year-to-year changes in groundwater level. Indeed, we have seen in Section 4.1.1 that the groundwater levels were higher in 2016 and 2018 compared to 2015 and 2017 (though all were higher than before the eruption). A one-to-one correlation between groundwater level and either precipitation or temperature is not observed, because variations in water table are a consequence of a variety of factors. Annual differences may be due to differences in the volumes of snow and ice that accumulated each year prior to melting (especially on Askja and Vaðalda), possible dust storms or volcanic eruptions depositing ash or dust on the glacier, and atmospheric conditions over the summer months (e.g., temperature, cloud cover/insolation, humidity, precipitation, wind, etc.). Finally, changes in glacial stream organization may also have a profound effect by altering the proportion of available water being transported by fluvial versus groundwater systems.

Fig. 8. Location of the hydrology measurements taken in the hot springs region in 2016, 2017, and 2018. Temperature is shown where available. All corresponding data and coordinates are given in Appendix B. The transects are numbered for reference in Tables B1–B3. (a) Map of the sUAS and field data gathered in the hot springs region during July 2016. In 2016, temperature and velocity were measured at select points, and the depth profile across each stream was measured independently. Consequently, the temperature and velocity are only an approximation at the location of the transects. The background is a 4 cm/pixel orthoimage taken on 7/30/2016 using the Trimble UX5-HP. (b) Map of the sUAS and field data gathered for the same region during July 2017. In 2017, water temperature and velocity were measured within each cross-section. The background is a 2–3 cm/pixel orthoimage taken on 7/25/2017–28/2017 using the DJI Phantom 4 Pro quadcopter. (c) Map of the sUAS and field data gathered in the hot springs region during August 2018. In 2018 also, water temperature and velocity were measured within each cross-section. The background is a 4 cm/pixel orthoimage taken on 8/3/2018 using the Trimble UX5-HP. Note the glacial stream in transect #1 has highly variable temperature, which are therefore not shown here.

Table 2
May–September values of the total monthly precipitation, for the years when data was taken. Data is from ERA-Interim, which are a combination of worldwide model predictions and nearby surface and satellite observations, and are given for the approximate location of the 2014–2015 Holuhraun lava flow-field (64.875°N, 16.500°W). See Section 3.4 and Dee et al. (2011) for details on this dataset.

	Total monthly precipitation (mm)				
	2003	2015	2016	2017	2018
May	67.9	72.8	27.2	116.7	105.9
June	71.3	42.7	40.6	87.0	60.9
July	113.3	88.5	70.2	54.3	76.9
August	44.4	126.6	81.7	42.2	89.6
September	82.2	91.0	158.6	178.0	82.5

Table 3
May–September values of monthly mean of daily mean temperature, for the years when data was taken. The standard deviations, which are large because of day/night cycles, are also given. Data is from ERA-Interim, which are a combination of worldwide model predictions and nearby surface and satellite observations, and are given for the approximate location of the 2014–2015 Holuhraun lava flow-field (64.875°N, 16.500°W). See Section 3.4 and Dee et al. (2011) for details on this dataset.

	Monthly mean of daily temperature (°C)				
	2003	2015	2016	2017	2018
May	-1.6 ± 3.8	-2.7 ± 3.8	-0.5 ± 3.2	1.9 ± 2.7	0.3 ± 3.1
June	2.7 ± 2.0	1.3 ± 2.4	3.8 ± 2.2	1.8 ± 1.9	3.4 ± 2.4
July	4.1 ± 2.4	2.1 ± 1.4	2.9 ± 1.8	3.7 ± 2.0	3.7 ± 1.7
August	3.9 ± 1.7	2.9 ± 1.7	2.8 ± 1.8	2.2 ± 2.0	2.1 ± 2.0
September	0.6 ± 3.6	2.3 ± 2.0	1.2 ± 2.3	2.4 ± 2.1	0.0 ± 2.7

4.2. Effects of continuous processes

Continuous processes causing hydrological changes around the Holuhraun lava field appear to be related to two interlinked causes: daily variations in meltwater discharge/generation from the glacier, and the subtle changes in the level of the groundwater table at Svartá and at the distal end of the 2014–2015 Holuhraun lava flow-field over longer periods of time. Among the annual changes described in Section 4.1.1, the expansion of seepage channels, the variations in glacial melt contribution, and the small reorganization of the channel morphologies are caused by continuously acting agents of change.

During the 2016 field campaign, we obtained high-resolution sUAS images of the same area on two different days and at two different times of the day, allowing us to observe small, continuous changes in action. The 1 cm/pixel imagery over the hot springs region was taken on July 28, and the 4 cm/pixel imagery was taken on July 30–31. Four different types of changes were observed: modifications in the braided stream morphology (Fig. 9a), channel bank erosion (Fig. 9b), different water levels in the incoming glacial river (Fig. 9c), and finally a single instance of seepage channel headward expansion (Fig. 9d). The difference in water level (Fig. 9c) observed in the newly entrenched glacial stream is due to the time at which the orthoimagery was taken in that area: around 10:30 AM on July 28 and around 6:00 PM on July 30, 2016. During the summer, the water level in the Jökulsá á Fjöllum river increases as the day progresses and the ice melted by the incoming solar radiation travels from the Vatnajökull glacier to the region of interest.

Morphological changes (Fig. 9a), including channel bank erosion (Fig. 9b), are expected within braided streams, especially during periods of high discharge (Goff and Ashmore, 1994). Indeed, the lack of vegetation, regular removal of fines in suspension within the flow, and the frequent fluctuations in water level make proglacial braided streams particularly unstable (Maizels, 2002). An added factor of instability at the time of our observations is the recent dam-bursting event, which occurred a week earlier, on July 21–22, 2016 (Sigurður (Siggi) Erlingsson, personal communication, 2016). This event drastically modified the local braided stream morphology, with the system continuing to seek a new equilibrium.

The seepage channel expansion observed between July 28 and July 30, 2016 (Fig. 9d) is caused by groundwater sapping. This process may have been enhanced by a local rise in the groundwater table following the dam-breaching event approximately one week before, which supplied more water to the area. Similarly, the new seepage activity seen in 2015 and 2016 to the north of the lava flow is also the result of groundwater sapping progressively eroding the riverbank.

4.3. Effects of catastrophic processes

4.3.1. Dam-breaching event: chronology

The eastern lava-dammed lake (Fig. 3c) was formed by glacial streams, which used to feed the Jökulsá á Fjöllum and became dammed by the 2014–2015 Holuhraun lava flow-field. It was located approximately 4 km to the southwest of the hot springs. On September 8, 2015, it covered an area of approximately 0.25 km^2, but its water level varied daily. This lake was essentially stable in its location until July 2016. The sequence of events leading to glacial water pouring into the

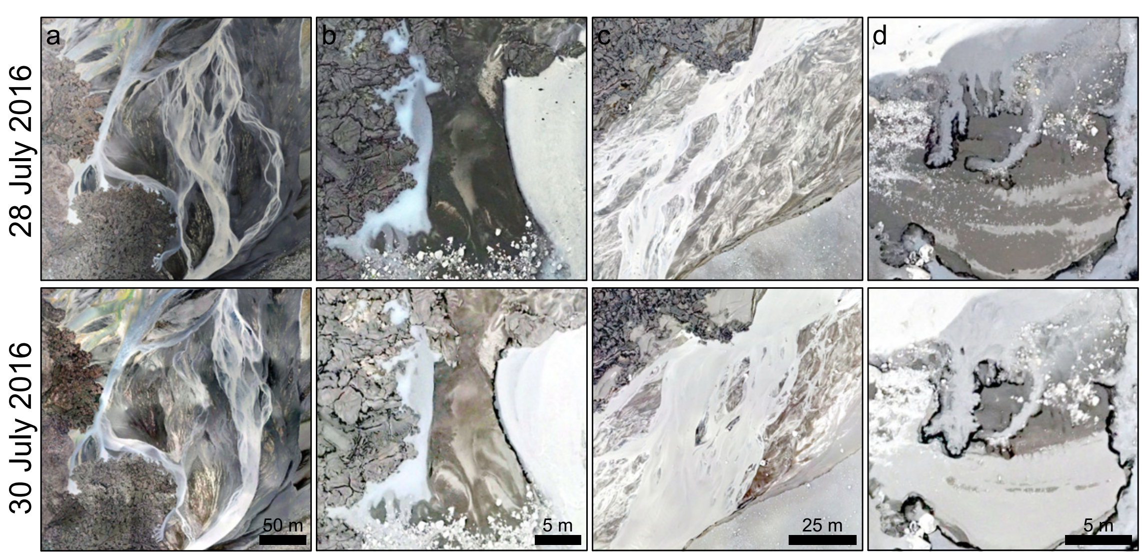

Fig. 9. Changes observed between July 28 and July 30, 2016. Top: 1 cm/pixel orthoimage acquired by a Trimble UX5-HP sUAS on July 28. Bottom: 4 cm/pixel orthoimage using the same sUAS on July 30. (a) Braided stream morphological changes. (b) Channel bank erosion. (c) Water level variations in the glacial river. (d) Seepage channel development.

hot springs is described below and is illustrated for a small part of the lava flow margin in Fig. 10, and for a larger region in Fig. 11.

In 2015, the water that had accumulated over the summer caused a minor outflow, entrenching a small channel along the edge of the lava flow (Fig. 10c). However, water from this event never reached the main channel in the hot springs region, but instead percolated into the ground and the lava, allowing the lake to retain its overall stability. Water continued to accumulate in the dammed lake in summer of 2016, until it breached into the hot springs in July 2016. Timing of the 2016 dam-breaching event, described here, was constrained by the eye-witness account of rangers within the Vatnajökull National Park (Bonnefoy et al., 2017). On July 15, 2016, a small trickle of water developed along the southeastern side of the flow. This glacial water from the lake met with another glacial stream (Fig. 11, Location 3). Together they breached into the hot springs on July 21 by creating a relatively small gap through the old riverbank (Fig. 11, Location 4; also visible in Fig. 6c). The main phase of the breach occurred on July 22, when glacial water began flowing into the hot springs with large waves pouring through this gap next to the lava. On July 22 and 23, a huge steam plume was seen rising from the location of the former lake, probably caused by large amounts of water flowing into new, still-hot regions of the lava. After the breach, water primarily flowed along the edge of the lava, but observations of water flowing through pools in the lava and from the springs located at the distal flow margin imply that some water continued to flow through and beneath the lava. After July 22, glacial stream water and water from the hot springs merged to produce braided network streams with a wide range of temperatures.

4.3.2. Dam-breaching event: magnitude and consequences

The new stream eroded by the dam-breaching event of July 22, 2016 is 20–70 m wide and 2 km long. Fig. 11 shows that a depth of at least 5 m of sediment was carried away as it excavated the new channel. The channel was modified during and after the dam breaching event, for example by stream bank erosion and sediment deposition: the maximum erosion depths during the breach are therefore unknown. Furthermore, significant amounts of sediment were deposited on top of the lava (Fig. 11), which in places was topographically lower than the surface of the adjacent sandsheet. Exact sediment volume deposited on the lava cannot be calculated as the river now flows on top of the lava in several places.

Flow velocity and discharge rate vary with the width and depth of the channel. Locations of sedimentation (e.g., profiles A to A' and C to C' in Fig. 12) cannot be used to estimate the original depth and width of the flood: the water velocity was lower in these places and entrained

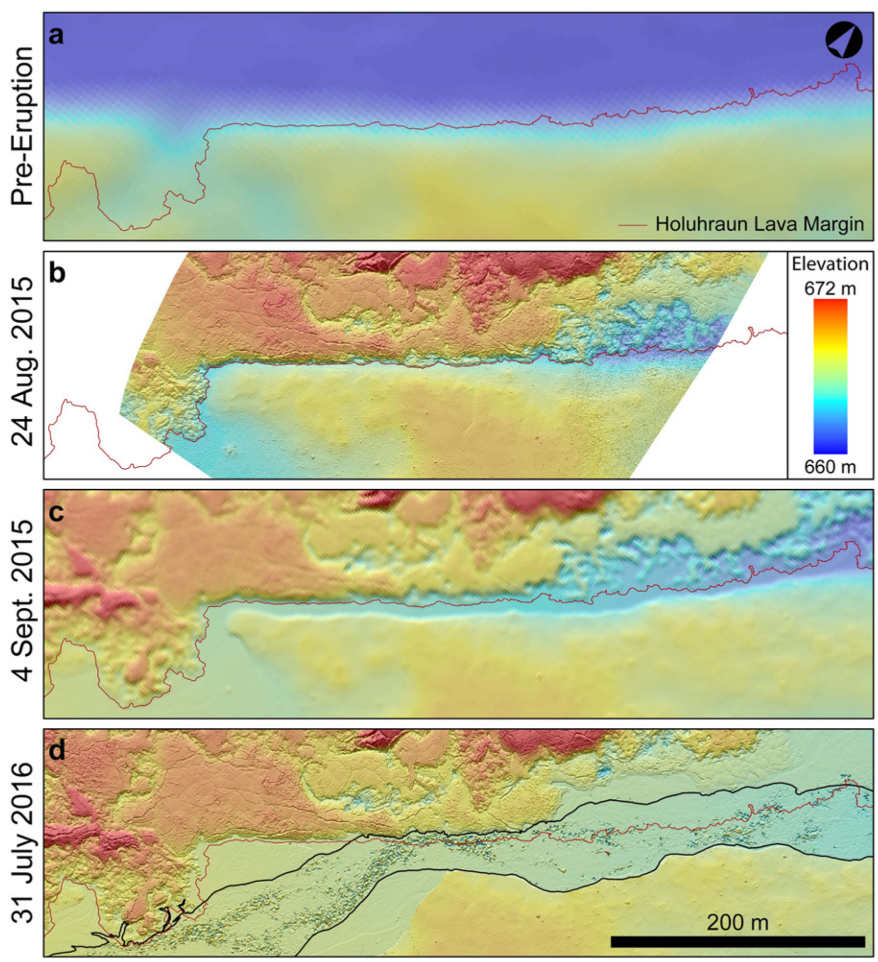

Fig. 10. Evolution of the region just downstream of the lake that breached in 2016. (a) Topography showing the right bank of a branch of the Jökulsá á Fjöllum river prior to the emplacement of the 2014–2015 Holuhraun lava flow-field. The riverbank was about 10 m high at this location. (b) In 2015, lava entered the river channel and abutted against its banks. (c) Between August 24 and September 4, 2015, the lake which had formed just west of this region overflowed, causing both erosion and some sediment deposition. The water did not reach the main channel, and the landscape is dry on September 4. (d) Water from the lake developed an overland flow toward the hot springs region forming a connection on July 21, 2016. A major dam-breaching event then occurred on July 22, 2016, transporting large amounts of sediment into the river and onto the lava flow. A branch of the Jökulsá á Fjöllum, outlined in black, now goes through this region, including on top of the lava. Note that reflections on the water within the Jökulsá á Fjöllum causes large amounts of noise in the resulting MVSP-derived DTM. (For interpreation of the references to color in this figure legend, the reader is referred to the web version of this article.)

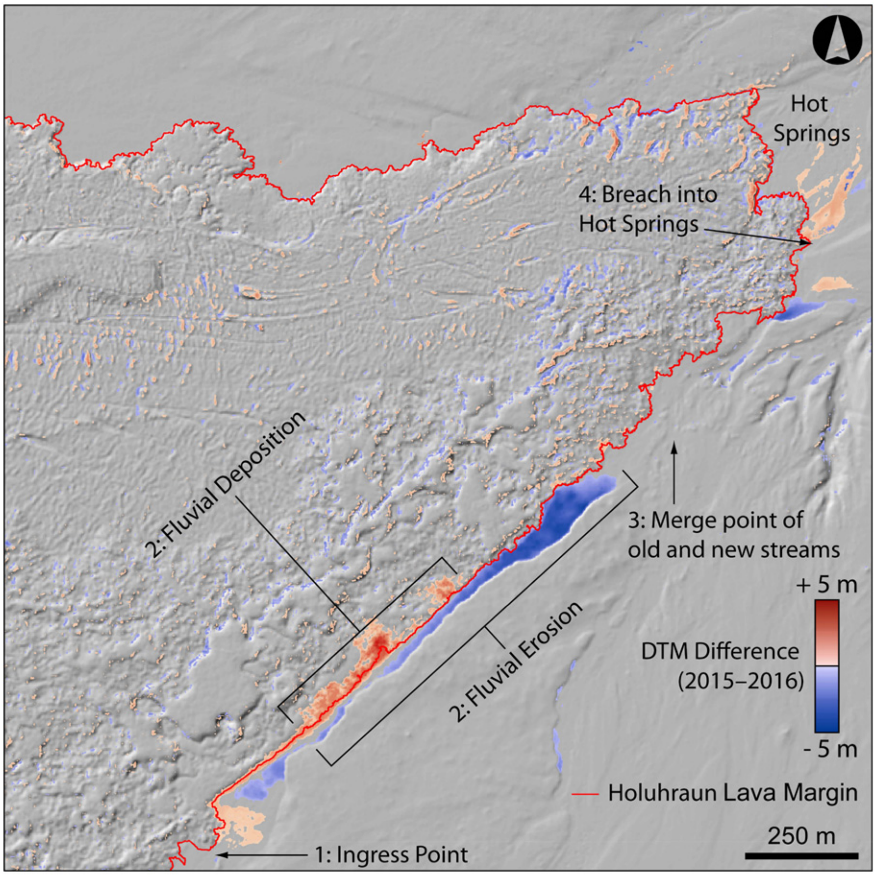

Fig. 11. Elevation changes from 2015 to 2016 in the hot springs region, obtained by subtracting the 2015 topography (NERC LiDAR and Loftmyndir photogrammetry; 2–5 m/pixel) from the 2016 topography (Trimble sUAS DTM; 20 cm/pixel), degraded to the same resolution. Elevation changes smaller than ± 0.7 m are not shown. The background is a hillshade created from the 20 cm/pixel DTM taken in 2016. The outline of the 2014–2015 Holuhraun lava flow is shown in red. The apparent small elevation changes within the lava flow-field are not real: they are due to small errors in the georeferencing of the DTMs. The sequence of events of the dam breach is indicated. 1: The lake breached approximately at this point. 2: The dam breaching event entrenched a new channel and deposited sediment onto the lava. 3: The new stream running along the lava merged with the older stream, which reached this point through another route. 4: The added water was enough to breach through the old riverbank and into the hot springs.

sediment was deposited, changing the morphology of the channel during the flood. Profiles where either the flood ran through an existing channel shape (e.g., profile B to B' in Fig. 12) or entrenched an entirely new channel (e.g., profile D to D' in Fig. 12) are used to estimate the width and depth of the channel for water velocity and discharge rate calculations. Using these profiles and assuming the channel was brim full, we estimate a flow velocity of 6.2 ± 0.3 m/s, giving a discharge of 1200 ± 250 m^3/s just downstream of the breach. This discharge is two to three orders of magnitude larger than the total discharge from the hot springs (2.2–14.0 m^3/s, Table 1), explaining how effective the dam-breaching event was for both erosion and sediment transport.

Sediment deposition on top of the lava and redirection of the river in 2016 caused a retreat of the visible lava margin compared to that of 2015. There are two regions where we have imagery of ≤4 cm/pixel in the summers of both 2015 and 2016: the hot springs region (Fig. 6) and the dam-breaching region (Fig. 11). Comparing the lava margin in 2015 and 2016 shows that 7421 m^2 of lava have been covered by sand and/or water. In contrast, the northern margin of the lava, which is not in contact with an active branch of the Jökulsá á Fjöllum, shows no such retreat of the visible lava flow margin.

5. Discussion

5.1. Origin of the hot springs

After the end of the Holuhraun eruption in February 2015, glacial meltwater ponded at the entry points into the lava, causing the formation of two lakes banked against the lava flow: one in the west, and the other in the east—relatively close to the hot springs region (Fig. 3). The lava is the main outlet for these lakes, and it is likely that most of the warm water forming the hot springs came from these lakes after taking different paths through the lava. After the eastern lake drained into the hot springs region in 2016, its contribution to water flux through the lava has greatly decreased, leaving the western lake as the main source of heated water for the hot springs. Given that the western lake is further from the hot springs than the eastern lake (12.1 km vs. 2.8 km), the hot springs take more time to respond to changes in the western lake. Thus, even though the lake is primarily controlled by glacial melt, the flux at the hot springs is not expected to be directly correlated to the time of day or to weather conditions. Additionally, as the lava flow cooled from above and below, residual heat concentrated within the core of the flow and was only able to warm the water when the depth of the water table approached the portions of the flow that were still hot. Consequently, when the eastern lava-dammed lake failed and drained in late July 2016, the water table would have locally lowered, thereby reducing the temperature of the water emerging from the hot springs until the groundwater table gradually increased in late August to early September.

5.2. Origin of the seepage channels

The development of seepage channels shown in Fig. 6 can be explained with several interacting processes responsible for the reorganization of the groundwater flow: changes in the level of the water table, a

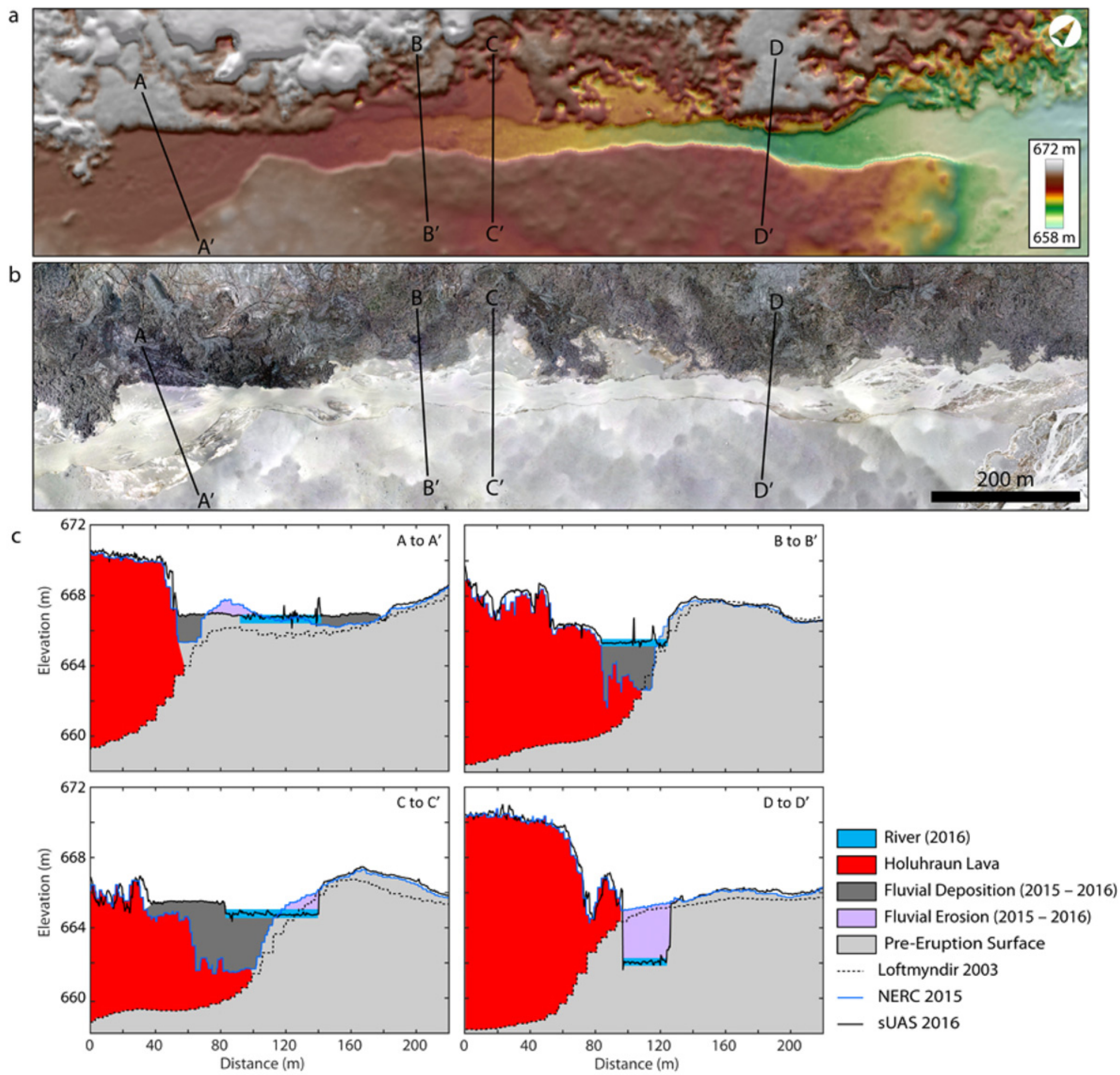

Fig. 12. We show (a) the 4 cm/pixel 2016 sUAS DTM, and (b) the 4 cm/pixel 2016 sUAS orthoimage, of the lava flow margin downstream of the lava-dammed lake that breached on July 22, 2016, one week after the breach. Elevation profiles were taken every meter along the new bed of the Jökulsá á Fjöllum river; four of these profiles are taken as examples. (c) Topography profiles are taken from the following datasets: the 2003 DTM from Loftmyndir ehf., the 2015 Lidar data from NERC, and the 2016 DTM from the Trimble UX5-HP sUAS. The lava, older glacial sediment, and position of the river in 2016 are shown. Regions of confirmed sediment deposition and erosion having occurred during the dam breaching event (i.e., between the time the 2015 and 2016 data were taken) are pointed out. Note the sUAS data is noisier in the river due to reflections from the water in the images. The 2003 DTM may be offset by ±0.5 m in this region (see Appendix A). Of these four examples, flood channel depth and width can only be estimated for profiles B to B' and D to D' (on the right).

reorganizing of the groundwater flow, development of artesian springs, escape of lava-heated water, and/or the formation of a layer of reduced permeability under and around the lava. In all cases, the springs that form will have the morphology of seepage channels, because the surface consists of unconsolidated sediment. Some of the groundwater emerging at the seepage channels probably percolates into the lava, but since the lava is already saturated with water, most of it forms small streams flowing along the margin of the lava toward the hot springs (Fig. 13b).

Variations in seepage activity in 2015–2018 affecting simultaneously Svartá (Fig. 4) and seepage channels near the hot springs (Fig. 6) suggest variations in the water table at distances of up to 2 km from the lava flow-field. As detailed in Section 4.1.3, the baseline groundwater level may be responding to annual differences in glacial melt from Vatnajökull as well as snowmelt from more local sources such as the Askja massif and Vaðalda. Thus, weather patterns may explain yearly changes (higher groundwater levels in 2016 and 2018), but they are insufficient to account for the long-lasting rise in water table after the eruption. A possibility we considered is a pulse of glacial melt from the eruption slowly moving through the groundwater system, which is supported by the presence of ice cauldrons indicating subglacial eruptions (Reynolds et al., 2017). However, the water level would then be expected to fall back after the meltwater travels through the groundwater system. Furthermore, Reynolds et al. (2017) estimate that only about 2.3×10^7 m^3 of ice melted during these subglacial eruptions. For comparison, this corresponds to five days of winter flux of the Jökulsá á Fjöllum through Upptyppingar (discharge rate of 55–60 m^3/s, Gylfadóttir, 2016), and it would thus contribute little to the aquifer.

Our preferred interpretation of the surface and groundwater flow before and after the 2014–2015 eruption is illustrated schematically in Fig. 13. It is likely that both before and after the eruption there is an aquifer carrying groundwater from the area of the Dyngjujökull glacier toward the northeast, flowing below the old bed of the Jökulsá á Fjöllum and the 2014–2015 Holuhraun lava flow (Baldursson et al., 2018). Lake

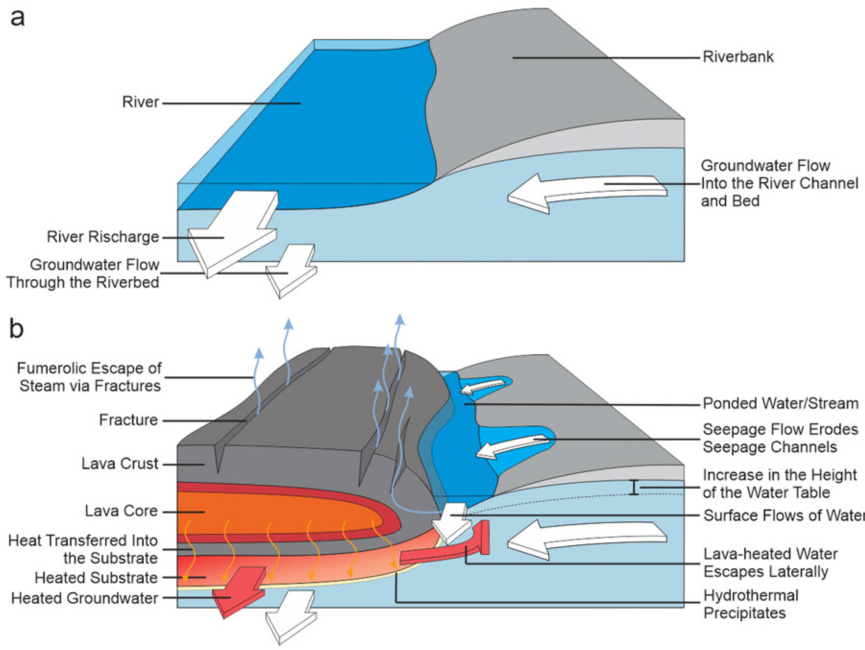

Fig. 13. Illustration of the surface and groundwater flow before and after the emplacement of the lava. (a) The river before emplacement of the lava flow. Seepage activity near the river was limited before the eruption and is not included here. (b) The lava was emplaced in the riverbed. The subsequent increase in the height of the water table caused ponding and the formation of seepage channels along the banks. The lava-heated water escapes both into the stream that forms along the bank, and at the distal end of the lava in the hot springs. A thin layer of hydrothermal precipitates might be present, isolating the groundwater flows inside and outside the lava.

Dyngjuvatn, the western lava-dammed lake, and snowmelt from Askja and Vaðalda may all contribute either to this aquifer, or to a shallower groundwater system, though it is impossible to identify the dominant source of water feeding Svartá and the hot springs without a dedicated study. Nonetheless, springs were known to exist within the bed of the Jökulsá á Fjöllum before the 2014–2015 eruption, supplying about 20 m^3/s to the river (Baldursson et al., 2018; Esther Hlíðar Jensen, personal communication, 2018). The area where this groundwater emerged is now covered in lava preventing the groundwater from entering the old riverbed (Fig. 13b). The portion of the water that would otherwise occupy the former river channel is then displaced into the adjacent groundwater system, raising the water table.

The emplacement of lava into the riverbed also had subtler effects on the groundwater flow. Indeed, a slight rise in the water table around the lava focused water into the topographic low formed between the pre-eruption topography and the lava creating a new small channel running parallel to the northern lava flow margin (Fig. 13b). The lava-dammed lakes also probably have an important role in the local water table. We infer from our observations that the water entering the groundwater system from the western lake both flows through the lava flow and spreads out along the left bank of the former river channel to supply water into the adjacent part of the sandsheet. This additional groundwater supply in and near the lava may have contributed to the elevated level of seepage channel activity observed near the lava. This hypothesis is supported by eyewitness observations by the authors and local park rangers, which suggest a correlation between high water levels in the western lava-dammed lake and increased seepage activity about a day later. However, the phase lag introduced by surface runoff entering into the groundwater system through the lava-dammed lake complicates straightforward correlations. It is thus unclear how far from the lava the water from the western lava-dammed lake can affect the groundwater system, and whether or not it could have affected Svartá.

Galeczka et al. (2016) documented an increase in activity of cold-water springs near the lava front after the eruption, and attributed it to an increase in the subsurface water pressure under the weight of the lava flow. However, we only observed artesian fountaining during the warmest days of August 2017, probably caused by a rapid rise in the water table (Section 4.1.1). This implies that short-term changes in the supply of glacial melt water also have an impact on the development of transient artesian fountains. An artesian system, with the aquifer being constrained either by the 2014–2015 lava or by much older lava, likely plays a role in the seepage channel expansion, but cannot explain the changes in activity 2 km away at Svartá.

Hydrothermal precipitates (e.g., carbonates, sulfates, and/or silicates) may have filled the pore spaces in the subsurface, thereby reducing the permeability of the surrounding substrate and modifying groundwater flow (Fig. 13). The water going through the lava, aided by the high temperatures within, dissolved the components of the basalt and as these hydrothermal fluids entered the substrate and formed precipitates. Indeed, Galeczka et al. (2016) found the water samples at the lava front to be supersaturated with respect to Al-bearing secondary phases including gibbsite, imogolite, kaolinite, and Ca-montmorillonite. If this supersaturated water entered the sandy/gravelly groundwater system and cooled down, these secondary phases could precipitate out of the water, filling the pore spaces. The layer of reduced porosity could then affect the path of subsurface water flow and contribute to the formation of seepage channels. Such a layer could reduce the exchange of groundwater going through the lava with that going under and around the lava. However, a low-permeability layer alone could not cause the observed changes in water level, so we do not consider it to be a dominant driver of hydrological change in this region.

It is likely that a rise in the water table represents the primary cause of increased seepage channel activity near the lava flow margin in 2015–2016. However, small artesian springs and changes in the permeability of the substrate beneath the lava by hydrothermal precipitation may have accelerated the formation of seepage channels. Indeed, an artesian pressure system would be particularly effective in enhancing seepage erosion at times when the groundwater table is higher, and a low permeability layer beneath the lava could reduce the flow of water into the former river channel bed, thereby directing flow toward the surface in regions adjacent to the lava. These processes may therefore have contributed to feedback mechanisms that enhanced seepage erosion.

5.3. Continuous versus catastrophic processes

Although most geologic work is done by large, catastrophic events rather than low-amplitude, continuous processes, the relative contributions of catastrophic versus incremental or continuous processes remain debated (Melosh, 2011). The 2014–2015 Holuhraun eruption initiated both catastrophic and continuous processes of landscape evolution.

The largest hydrological changes in the region, including erosion and sediment deposition of up to 5 m, were brought about by the 2016 dam-breaching event, as a new riverbed was entrenched along the margin of the lava flow (Section 4.3). The discharge rate during the breach was over two orders of magnitude larger than the normal discharge rate in the hot springs in the same year, but was concentrated to a channel only tens of meters across. The large area of lava covered by sediment is especially significant as it illustrates the first major step in the degradation of a lava flow. The dam-breaching event also modified the morphology and the temperature distribution in the hot springs region (Section 4.1).

Continuous processes, however, have also caused appreciable change in the region over only three years. The first snowmelt after the end of the eruption may have had the largest contribution to the partial burial of lava flow margins, which appear to have already been mantled in sediment by the time the first aerial images were acquired in August 24, 2015. Subsequent snow melts, rainfall, and aeolian sediment transport do not appear to have had significant erosional or depositional effects in the region of interest over our timescale of observation. The continuous movements of the braided stream, due mainly to daily changes in glacial melt, cause a regular redistribution of the channels and terraces, though these changes have low preservation potential. Daily and yearly changes in groundwater flow have contributed to the development of new seepage channels in the hot springs region through headward erosion and the redistribution of sediments. While having very low discharge, the area covered by active seepage channels increased by a factor of fifteen over the first eighteen months following the end of the eruption, although the topography difference is mostly below the resolution of the DTMs. Although groundwater seepage decreased in 2017, the topography created by this process during the two previous years remains, indicating that the change in the landscape may be long-lasting. Contributions to landscape evolution by catastrophic and continuous processes are therefore very different, but both appear to be important to our understanding of the hydrology in the region.

5.4. Implications for Mars

Groundwater seepage, weakening bedrock through chemical and physical weathering processes, may also have formed theater-headed valleys on Mars (Baker et al., 1990, 2015; Goldspiel and Squyres, 2000; Gulick, 2001; Harrison and Grimm, 2005; Mangold et al., 2008), though other processes may also be able to form similar morphologies (Howard et al., 2005; Lamb et al., 2006; Luo and Howard, 2008). While the groundwater seepage interpretation remains under debate for large theater-headed valleys such as Nirgal Vallis or parts of Vallis Marineris (Lamb et al., 2006; Luo and Howard, 2008; Mangold et al., 2008; Pelletier and Baker, 2011; Marra et al., 2015), it is possible that groundwater seepage played a role in the formation of smaller channels in cohesionless sediments during Mars's early, wet history, though these channels would have been largely eroded by now (Craddock and Howard, 2002; Luo and Howard, 2008). Recently, Pendleton (2015) and Nahm et al. (2016) invoked groundwater seepage to explain very young theater-headed channels in the source region of the Athabasca Valles flood lava flow. These features, also described by Balme and Gallagher (2009), are morphologically similar to seepage channels on Earth such as the ones by the Holuhraun lava flow-field, but are difficult to reconcile with their occurrence in a geologically young (<20 Ma) lava-mantled Martian setting (Berman and Hartmann, 2002; Jaeger et al., 2010). Our direct observations of the changes wrought upon groundwater seepage by a lava flow at Holuhraun may serve as a useful analog to shed light upon Martian seepage channels.

The Dyngjusandur region provides an excellent analog for Mars (Hamilton, 2015; Richardson et al., 2018), and even before the 2014–2015 eruption, it has been compared to sandsheets on Mars (Baratoux et al., 2011). These similarities stem from the high altitude, low temperature, prevalence of basaltic sand, and almost complete lack of vegetation at Dyngjusandur. Though much smaller, the 2014–2015 Holuhraun lava flow-field is also a good analog for Martian flood lava flows (Voigt et al., 2017), such as the recent (<20 Ma) low-viscosity basaltic flood lavas having erupted from the Cerberus Fossae in Athabasca Valles, Rahway Valles, Marte Vallis, or Amazonis Planitia (Lanagan et al., 2001; Fuller and Head, 2002; Voigt and Hamilton, 2018). Future studies would therefore benefit from using the Holuhraun seepage channels as an analog to morphologically similar landforms in volcanic settings on Mars.

6. Conclusions

The emplacement of the 2014–2015 Holuhraun lava flow-field modified the landscape and affected the local hydrology in a variety of ways. The lava was emplaced onto part of the Jökulsá á Fjöllum river's flood plain, infilling former stream channels and affecting the path of glacial melt water. Where active stream channels were blocked by the flow margin, lava-dammed lakes formed. The water level within these lakes varied on a diurnal basis during the summer months, changing in response to rates of glacial melting. Much of the lake water percolated into the lava, cooling the lava flow and emerging from the flow front as hot springs. However, in 2016 the capacity of the lava-dammed lake located along the eastern margin of the flow was exceeded, which triggered overland water flow and ultimately a dam-breaching event on July 22, 2016. This flood caused sudden changes within the hydrological system and in erosion and sediment depositional rates. In addition to this catastrophic event as an agent of change, there were also continuous hydrological processes in the region that caused changes in the landscape. Cold seepage springs developed next to the lava flow margin and the level of water changed yearly within the existing seepage channel, Svartá, which is located 2 km away from the lava flow front. Temperature and precipitation records indicate that 2015–2018 was not an atypical period in terms of the decadal-scale weather patterns in the region, which suggests that the observed hydrological changes were caused by the emplacement of the 2014–2015 Holuhraun lava flow-field. We also conclude that the formation of lava-dammed lakes and the infiltration of water into the lava and surrounding substrate affected seepage channel activity, water-enhanced lava cooling rates, and hot springs temperatures. Following the collapse of the eastern lava-dammed lake, the western lake likely provides the dominant control over local hydrological processes. Therefore, monitoring hydrological and landscape evolution processes associated with the 2014–2015 Holuhraun lava flow-field provides a rare opportunity to document how environments respond to large basaltic lava eruptions, and it provides an exceptional ground-truth example crucial for interpreting the geologic record of volcanic landscapes on other planets, particularly on Mars.

Acknowledgements

The authors thank the Vatnajökull National Park Service (Vatnajökulsþjóðgarður) for access to the study region, Vatnajökull

National Park rangers for their help and hospitality at Drekagil, and Park Ranger Sigurður (Siggi) Erlingsson for many informative discussions relating to the changing environmental conditions within the Holuhraun region. We also thank Victor Baker for discussions related to hydrological processes and others who assisted our team in the field. Specifically, we would like to thank Laszlo Keszthelyi and Colin Dundas (2015), Joana Voigt and Kristina Lincoln (2016), Muhammad Aufaristama and Alma Gytha Huntington-Williams (2017), and Sarah Sutton and Jennifer Eigenbrode (2018). The IsViews project (Iceland subglacial Volcanoes interdisciplinary early warning system), funded by the Bavarian Ministry of Economic Affairs and Media, Energy and Technology (ID 20-8-34102-15-2012), is gratefully acknowledged, as well as the German company GeoFly acquiring and processing the airborne UltraCam-Xp data for IsViews. Agúst Gudmundsson, Fjarkönnun ehf. is gratefully acknowledged for his support with the organization and management of UltraCam-Xp camera flights. We also thank the Icelandic Research Center (Rannsóknamiðstöð Islands) for granting fieldwork permits (2014–2018) as well as the director of the Vatnajökulsþjóðgarður, Þórdur H. Ólafsson for the special permit at Holuhraun. Finally, the authors thank Ingrid Utskins as well as two anonymous reviewers for their detailed and helpful reviews, which led to significant improvement of this paper. Funding support was provided by NASA Planetary Geology and Geophysics Grant # NNX14AL54G, and the University of Arizona's Carson Graduate Fellowship program.

Appendix A. Coverage and resolution of airborne remote sensing data

In our study, we use airborne remote sensing data collected during the summers of 2003, 2013, 2015, 2016, 2017, and 2018. These data are described in Section 3.1 and detailed information is given in Table A1. Fig. A1 shows the extent and resolution of the pre- and post-eruption datasets covering the entirety of the Holuhraun lava flow-field.

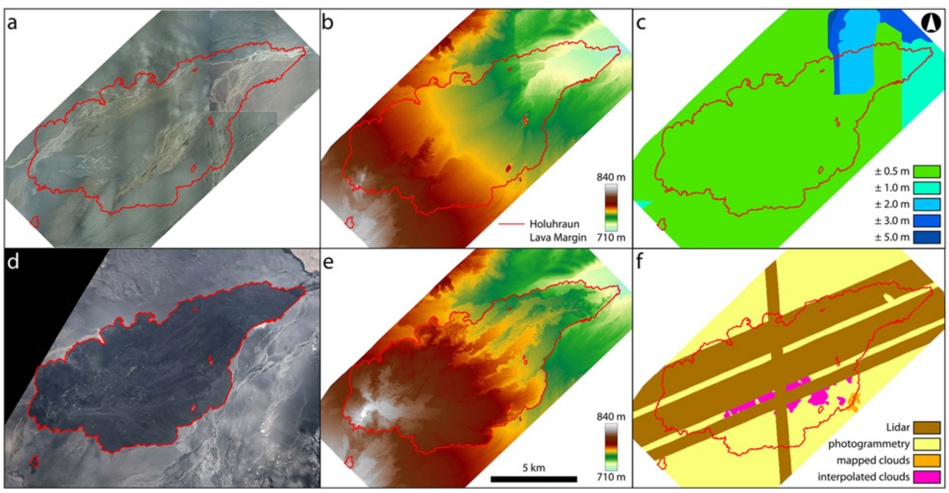

Fig. A1. Top: Pre-eruption dataset, taken in August 2003 and August 2013 and processed by Loftmyndir ehf. Bottom: Post-eruption regional dataset, dating from August 2015. This dataset includes data from NERC, Loftmyndir ehf., and the IsViews Project.

Table A1
Characteristics of the aerial data used.

Year	Date	Data type	GSD	Areal coverage	Platform	Processed
2003	23 Aug.	Orthophoto-mosaic DTM	50 cm 5 m	35.6 km^2; future hot spring region	Airborne photogrammetry	Loftmyndir ehf.
2013	12 Aug	Orthophoto-mosaic DTM	50 cm 5 m	130.6 km^2; lava field and surroundings	Airborne photogrammetry	Loftmyndir ehf.
2015	24 Aug.	Orthophoto-mosaic DTM	4 cm 16 cm	0.14 km^2; dam breaching region	sUAS (Phantom 3 Pro)	Pix4D
	30 Aug.	Orthophoto-mosaic DTM	50 cm 5 m	167 km^2; lava field and surroundings	Airborne photogrammetry	Loftmyndir ehf.
	4 Sept.	DTM	2 m	100 km^2; partial coverage of lava field and surroundings	Airborne LiDAR	NERC
	4 Sept.	Orthophoto-mosaic DTM	4 cm 16 cm	0.24 km^2; hot spring region	sUAS (Phantom 3 Pro)	Pix4D
	8 Sept.	Orthophoto-mosaic	20 cm	837 km^2; lava field, Vaðalda, Svartá, Askja, Vatnajökull	Airborne UltraCam	IsViews, LMU Munich
2016	28 July	Orthophoto-mosaic DTM	1 cm 5 cm	0.96 km^2; hot springs region	sUAS (UX5-HP)	Trimble Business Center
	30–31 July	Orthophoto-mosaic DTM	4 cm 20 cm	8.2 km^2; hot springs region	sUAS (UX5-HP)	Trimble Business Center
2017	25–28 July	Orthophoto-mosaic DTM	2.3 cm 9 cm	0.76 km^2; hot springs region	sUAS (Phantom 4 Pro)	Pix4D
2018	3 Aug.	Orthophoto-mosaic DTM	4 cm 20 cm	8.2 km^2; hot springs region	sUAS (UX5-HP)	Trimble Business Center

Table A2
Precision of sUAS data products. Trimble UX5-HP data products are georeferenced using differentially corrected GPS data from an Trimble R10 base station and the UX5-HPs GNSS GPS receiver. The R10 system is capable of producing survey points with 0.8 cm horizontal precision and 1.5 cm vertical precision. Combined with the exact timing of the camera shutter, the positions of each image acquisition is known during the flight path and are therefore airborne control points. The mean standard deviations (at $\pm 1\sigma$) in the x, y, and z directions (i.e., latitude, longitude, and elevation) of terrain points for 2016 are estimated to be ±3.0 cm, ±4.0 cm, and ±6.4 cm, respectively. For 2018, these values are ±4.1 cm, ±3.1 cm, and ±5.8 cm, respectively. DJI Phantom sUAS surveys are coregistered using ground control tie points visible in 2016 UX5-HP orthoimage data; height values are obtained from the DTM. For co-registered Pix4D-processed surveys, the table below reports the mean root mean square error (RMSE) of terrain points as compared to control points used from 2016 UX5-HP orthoimage and DTM data.

Year	Day	Platform	Control method	No. of control points	RMSE (cm)
2015	24 Aug.	Phantom 3 Pro	Manual coregistration of tie points to 2016 UX5-HP data	7	10.6
2015	4 Sept.	Phantom 3 Pro	Manual coregistration of tie points to UX5-HP data	7	2.70
2017	25–28 July	Phantom 4 Pro	Manual coregistration of tie points to UX5-HP data	16	3.50

Appendix B. Hydrology analysis methods

B.1. 2016 hydrological analysis

In 2016, channels profiles were measured using a Trimble R10 DGPS, with ~3-cm-precision, which was used to sample the depth of the channel every 10–20 cm. A Hydrolab DS5 Multiparameter Data Sonde was used to measure a variety of parameters associated with each stream channel, including temperature and pH, which were measured with a precision of 0.01 °C, and 0.01 pH units, respectively. A General Oceanics, Inc. Environmental flow meter/velocity sensor was used to measure water flow velocity with a precision of 0.1 m/s. Water flux Q [m^3/s] was determined for each channel by calculating the channel cross-sectional area and multiplying by corresponding velocity measurement. Heat flux, E_{flux} [J/s], was then calculated using Eq. (2). In 2016, temperature and velocity data were taken on different days and in some places are offset from the transects. We therefore used the nearest velocity and temperature point within the same stream for each transect. Note that cross-sections #6 has no nearby temperature and pH measurement, and cross-section #1 has no nearby velocity measurement.

Table B1
Results of the field data gathered in the hot springs region between July 28 and August 4, 2016. If several temperature and velocity measurements were taken for a stream, the average is presented here. For cross-section #1, no velocity measurements were taken; we therefore calculated the velocity using Manning's equation, as described in Section 3.3. In cross-section #6, no temperature or pH measurements were taken. Given that cross-section #6 has the same water source as cross-section #7, we assume the same water temperature when calculating the heat flux. We also note that cross-section #1 is a mixture of cold springwater and water heated by the lava. See Fig. 6a for a map of these data. Latitude and longitude are referenced to the ISN2004 datum.

ID	Channel type	Cross-sectional area (m^2)	Temperature (°C)	pH	Velocity (m/s)	Discharge rate (m^3/s)	Heat flux (GJ/s)	Start longitude	Start latitude	End longitude	End latitude
1	Mixed	6.1	8.7	8.9	0.77[a]	4.7	5.56	−16.513326	64.932474	−16.513260	64.932737
2	Hot springs	2.1	14.8	8.8	0.92	1.9	2.31	−16.513303	64.932445	−16.513171	64.932347
3	Hot springs	3.2	16.9	8.7	0.47	1.5	1.81	−16.513937	64.931831	−16.514103	64.931936
4	Hot springs	2.6	16.7	8.7	0.71	1.9	2.26	−16.513638	64.931632	−16.513839	64.931738
5	Hot springs	3.5	13.5	8.8	1.15	4.0	4.87	−16.512978	64.931392	−16.513303	64.931451
6	Glacial	7.0	–[b]	–[b]	0.68	6.2	7.29	−16.511678	64.930236	−16.511928	64.930273
7	Glacial	8.4	5.7	7.8	1.25	8.6	10.16	−16.511529	64.929794	−16.511335	64.929609

[a] Calculated.
[b] No data available; we assume the same values as for stream #7.

B.2. 2017 hydrological analysis

In 2017, stream profiles were also measured, but in a different way to account for variable conditions across the streams. For each stream cross-section shown in Fig. 8b, stream depths were measured using a tape measure at regular intervals, ranging from 20 cm to 1 m, with depth measurements rounded to the nearest centimeter. For each measured segment along the stream profile we measured temperature and pH using an Ecosense pH10A Handheld pH/Temperature Pen Tester, which has a precision of 0.01 °C, and 0.01 pH units, respectively. Stream flow velocities were measured with Global Water Flow Probe, with a precision of 0.1 m/s. We then calculated Q and E_{flux} in each segment of the stream (see Eqs. (1) and (2)), which we then summed to obtain the total discharge rate and total heat flux through each stream.

Table B2
Results of the field data gathered in the hot springs region in July 2017. If several temperature and velocity measurements were taken for a stream, the average is presented here. Cross-section #29 was too shallow for temperature and pH measurements to be taken. We also note that cross-sections #1, 4, 6, 7, 18, 20, and 26 are mixtures of cold springwater and water heated by the lava. See Fig. 8b for a map of these data. Latitude and longitude are referenced to the ISN2004 datum.

ID	Channel type	Cross-sectional area (m^2)	Temperature (°C)	pH	Velocity (m/s)	Discharge rate (m^3/s)	Heat flux (GJ/s)	Start longitude	Start latitude	End longitude	End latitude
1a	Cold spring	1.6	6.9	9.1	0.6	0.94	1.10	−16.513209	64.932716	−16.513205	64.932676
1b	Hot spring	1.7	9.1	9.0	0.5	0.83	0.99	−16.513205	64.932676	−16.513203	64.932635
2	Hot spring	2.4	11.5	8.9	1.08	2.58	3.08	−16.512697	64.932411	−16.512485	64.932362
3	Hot spring	0.3	7.0	9.1	0.27	0.08	0.10	−16.512253	64.930593	−16.512374	64.930549
4	Mixed	1.9	8.4	9.0	0.48	0.92	1.09	−16.514584	64.934238	−16.514668	64.93434
5	Hot spring	0.5	10.9	9.3	0.32	0.15	0.18	−16.517051	64.932611	−16.517029	64.932573
6	Mixed	2.0	9.7	9.1	0.34	0.69	0.82	−16.518366	64.932684	−16.518537	64.932744
7	Mixed	0.9	7.6	9.0	0.16	0.14	0.16	−16.52038	64.932597	−16.520503	64.932654
8	Cold spring	0.2	5.1	9.3	0.17	0.03	0.04	−16.521871	64.932533	−16.52174	64.932545
9	Cold spring	0.1	5.4	9.2	0.31	0.04	0.05	−16.522182	64.932658	−16.522124	64.932683
10	Cold spring	0.3	5.2	9.0	0.39	0.13	0.15	−16.516593	64.934205	−16.516454	64.934226

(continued on next page)

Table B2 (*continued*)

ID	Channel type	Cross-sectional area (m^2)	Temperature (°C)	pH	Velocity (m/s)	Discharge rate (m^3/s)	Heat flux (GJ/s)	Start longitude	Start latitude	End longitude	End latitude
11	Cold spring	0.6	5.2	9.0	0.49	0.29	0.34	−16.515407	64.934183	−16.515454	64.93414
12	Hot spring	0.7	5.9	9.2	0.88	0.59	0.69	−16.514435	64.932165	−16.514487	64.932195
13	Hot spring	0.5	8.9	9.0	0.62	0.33	0.39	−16.514224	64.932118	−16.514139	64.932108
14	Hot spring	0.7	9.1	9.0	0.20	0.13	0.16	−16.513993	64.931695	−16.513876	64.931695
15	Cold spring	0.2	5.1	9.1	0.35	0.06	0.07	−16.516398	64.933996	−16.51655	64.934083
16	Hot spring	0.3	7.2	9.2	0.33	0.11	0.13	−16.519472	64.93236	−16.519642	64.932379
17	Hot spring	0.5	7.1	9.2	0.33	0.15	0.18	−16.517808	64.932569	−16.517743	64.932625
18	Mixed	1.7	5.8	9.1	0.49	0.83	0.98	−16.513388	64.934368	−16.51351	64.934496
19	Hot spring	0.7	6.5	9.0	0.29	0.20	0.24	−16.513933	64.932489	−16.513998	64.932507
20a	Cold spring	2.2	5.3	9.2	0.7	1.55	1.81	−16.511968	64.932836	−16.511918	64.932758
20b	Hot spring	2.7	8.7	9.1	0.8	2.23	2.65	−16.511918	64.932758	−16.51189	64.932717
21	Hot spring	0.1	7.3	9.0	0.46	0.05	0.06	−16.512546	64.93059	−16.512694	64.930596
22	Hot spring	1.0	10.9	9.0	0.73	0.70	0.84	−16.514361	64.930492	−16.514213	64.93048
23	Hot spring	0.6	7.1	9.1	0.35	0.22	0.26	−16.513411	64.930778	−16.513464	64.930739
24	Hot spring	2.5	9.4	9.0	0.71	1.77	2.10	−16.513526	64.930952	−16.513711	64.930995
25	Hot spring	0.3	8.6	9.1	1.01	0.31	0.37	−16.513829	64.93069	−16.513848	64.930625
26a	Cold spring	1.3	4.5	9.2	0.24	0.31	0.36	−16.513894	64.932708	−16.513882	64.932685
26b	Hot spring	0.8	5.5	9.2	0.33	0.27	0.32	−16.513882	64.932685	−16.513872	64.93266
27	Cold spring	0.1	5.4	8.8	0.15	0.01	0.01	−16.515392	64.934214	−16.515326	64.934226
28	Glacial	2.6	4.9	8.0	1.13	2.90	3.40	−16.511816	64.929682	−16.511621	64.929597
29	Cold spring	0.0	–[a]	–[a]	–[a]	–[a]	–[a]	−16.522133	64.932535	−16.521952	64.932536

[a] Too shallow for the instruments.

B.3. 2018 hydrology analysis

In 2018, we used the same instruments as in 2017; however, having observed during the preceding years that the channel profiles were generally rectilinear, we simplified our approach to estimating cross-sectional area by simply calculating it as the product of depth and width. The only exception to this was the channel described by segments #24 and #25, which is located where a springwater and lava-filtered spring come together, as shown in Fig. 8c. In this case the channel exhibited a bimodal depth, temperature, and pH distribution, and we divided it into two segments. Q and E_{flux} were calculated for each channel as before using Eqs. (1) and (2).

Table B3

Results of the field data gathered in the hot springs region on August 11, 2018. Points #16–19 were taken in pools near the lava flow margin, and are not channels. Cross-section #1 has highly variable temperature, velocity, and water levels. See Fig. 6c for a map of these data. Latitude and longitude are referenced to the ISN2004 datum.

ID	Channel type	Cross-sectional area (m^2)	Temperature (°C)	pH	Velocity (m/s)	Discharge rate (m^3/s)	Heat flux (GJ/s)	Start longitude	Start latitude	End longitude	End latitude
1	Glacial	–[a]	6.6–10.5	7.7	–[a]	–[a]	–[a]	−16.511357	64.930070	−16.510601	64.929885
2	Hot spring	0.97	9.8	8.8	0.8	0.77	0.92	−16.514314	64.930438	−16.514237	64.930429
3	Cold spring	1.70	3.8	9.1	0.2	0.34	0.40	−16.514331	64.932696	−16.514260	64.932651
4	Hot spring	1.04	7.7	8.9	0.9	0.93	1.10	−16.511398	64.930083	−16.511498	64.930138
5	Hot spring	0.24	7.3	8.8	0.3	0.07	0.08	−16.512179	64.930488	−16.512109	64.930495
6	Hot spring	0.43	7.0	9.0	0.5	0.21	0.25	−16.512320	64.930539	−16.512264	64.930530
7	Hot spring	0.26	7.7	9.8	0.8	0.21	0.25	−16.512625	64.930594	−16.512534	64.930592
8	Hot spring	0.46	7.4	8.9	0.7	0.32	0.38	−16.512843	64.930700	−16.512889	64.930668
9	Hot spring	0.16	7.1	8.8	0.4	0.07	0.08	−16.512987	64.930645	−16.513028	64.930627
10	Hot spring	0.88	7.4	9.1	0.4	0.35	0.42	−16.513410	64.930786	−16.513492	64.930744
11	Hot spring	0.80	7.3	8.9	0.8	0.64	0.76	−16.513684	64.930631	−16.513636	64.930663
12	Hot spring	0.42	7.9	8.9	0.4	0.17	0.20	−16.513648	64.930584	−16.513568	64.930576
13	Hot spring	1.11	7.7	8.8	0.6	0.67	0.79	−16.513532	64.930573	−16.513459	64.930587
14	Hot spring	0.40	8.8	8.9	0.2	0.08	0.10	−16.514091	64.930588	−16.514049	64.930593
15	Hot spring	2.06	9.5	8.9	0.9	1.85	2.21	−16.514122	64.930617	−16.514230	64.930636
16	Hot spring	–[b]	9.1	8.9	–	–	–	−16.514220	64.930882		
17	Hot spring	–[b]	8.1	8.9	–	–	–	−16.514031	64.931854		
18	Hot spring	–[b]	7.7	8.9	–	–	–	−16.514357	64.931841		
19	Hot spring	–[b]	6.8	9.0	–	–	–	−16.514443	64.931872		
20	Hot spring	0.95	6.4	8.8	0.8	0.76	0.89	−16.514215	64.932133	−16.514101	64.932126
21	Hot spring	0.69	5.5	8.8	1.4	0.97	1.14	−16.514459	64.932204	−16.514396	64.932173
22	Hot spring	1.62	6.7	9.1	0.9	1.46	1.72	−16.513995	64.932326	−16.513935	64.932271
23	Hot spring	3.01	8.2	8.6	0.9	2.71	3.21	−16.513397	64.931490	−16.513041	64.931454
24	Hot spring	0.58	6.6	8.5	0.5	0.29	0.34	−16.513320	64.932666	−16.513296	64.932635
25	Cold spring	2.41	4.8	9.2	0.8	1.93	2.26	−16.513344	64.932708	−16.513320	64.932666

[a] Too variable to measure.
[b] Pool measurement, not transects.

References

Alho, P., Russell, A.J., Carrivick, J.L., Käyhkö, J., 2005. Reconstruction of the largest Holocene jökulhlaup within Jökulsá á Fjöllum, NE Iceland. Quat. Sci. Rev. 24 (22), 2319–2334. https://doi.org/10.1016/j.quascirev.2004.11.021.

Allen, M.B., Mark, D.F., Kheirkhah, M., Barfod, D., Emami, M.H., Saville, C., 2011. 40Ar/39Ar dating of Quaternary lavas in northwest Iran: constraints on the landscape evolution and incision rates of the Turkish-Iranian plateau. Geophys. J. Int. 185 (3), 1175–1188. https://doi.org/10.1111/j.1365-246X.2011.05022.x.

Arcement, G.J., Schneider, V.R., 1989. Guide for selecting Manning's roughness coefficients for natural channels and flood plains. United States Geological Survey Water-Supply Paper. vol. 2339 , pp. 1–38. http://pubs.er.usgs.gov/publication/wsp2339.

Arnalds, O., Dagsson-Waldhauserova, P., Olafsson, H., 2016. The Icelandic volcanic aeolian environment: processes and impacts—a review. Aeolian Res. 20, 176–195. https://doi.org/10.1016/j.aeolia.2016.01.004.

Aufaristama, M., Hoskuldsson, A., Ulfarsson, M.O., Jonsdottir, I., Thordarson, T., 2019. The 2014–2015 lava flow field at Holuhraun, Iceland: using airborne hyperspectral

remote sensing for discriminating the lava surface. Remote Sens. 11 (5), 476. https://doi.org/10.3390/rs11050476.
Bahr, Th., 1997. Hydrogeologische Untersuchungen im Skeidarársandur (Südisland). Diss., Münchner Geol. Hefte, B 3. Seiten 142–3.
Baker, V.R., Kochel, R.C., Laity, J.E., Howard, A.D., 1990. Spring sapping and valley network development. Special Paper of the Geological Society of America 252, 235–265. https://doi.org/10.1130/SPE252-p235.
Baker, V.R., Hamilton, C.W., Burr, D.M., Gulick, V.C., Komatsu, G., Luo, W., Rice Jr., J.W., Rodriguez, J.A.P., 2015. Fluvial geomorphology on Earth-like planetary surfaces: a review. Geomorphology 245, 149–182. https://doi.org/10.1016/j.geomorph.2015.05.002.
Baldursson, S., Guðnason, J., Hannesdóttir, H., Thórðarson, T., 2018. Nomination of Vatnajökull National Park for Inclusion in the World Heritage List. Vatnajökull National Park, Reykjavík.
Balme, M.R., Gallagher, C., 2009. An equatorial periglacial landscape on Mars. Earth Planet. Sci. Lett. 285, 1–2), 1–15. https://doi.org/10.1016/j.epsl.2009.05.031.
Baratoux, D., Mangold, N., Arnalds, O., Bardintzeff, J.M., Platevoet, B., Grégoire, M., Pinet, P., 2011. Volcanic sands of Iceland-Diverse origins of aeolian sand deposits revealed at Dyngjusandur and Lambahraun. Earth Surf. Process. Landf. 36 (13), 1789–1808. https://doi.org/10.1002/esp.2201.
Berman, D.C., Hartmann, W.K., 2002. Recent fluvial, volcanic, and tectonic activity on the Cerberus plains of Mars. Icarus 159 (1), 1–17. https://doi.org/10.1006/icar.2002.6920.
Bonnefoy, L.E., Hamilton, C.W., Scheidt, S.P., Voigt, J., Hoskuldsson, À., Jónsdottir, I., Thordarson, T., 2017. Landscape Evolution after the 2014–2015 Lava Flow at Holuhraun, Iceland. Lunar Planetary Science Conference. vol. 48 (Abstract 1652).
Bonny, E., Thordarson, T., Wright, R., Höskuldsson, A., Jónsdóttir, I., 2018. The volume of lava erupted during the 2014 to 2015 eruption at Holuhraun, Iceland: a comparison between satellite- and ground-based measurements. Journal of Geophysical Research: Solid Earth 123, 5412–5426. https://doi.org/10.1029/2017JB015008.
Cosyn, P., Miller, R., 2013. Trimble UX5 Aerial Imaging Solution – A New Standard in Accuracy, Robustness and Performance for Photogrammetric Aerial Mapping. White Paper. Trimble Navigation limited 7pp. Available online at. uas.trimble.com/media/downloads.
Cousins, C.R., Crawford, I.A., Carrivick, J.L., Gunn, M., Harris, J., Kee, T.P., Karlsson, M., Carmody, L., Cockell, C., Herschy, B., Joy, K.H., 2013. Glaciovolcanic hydrothermal environments in Iceland and implications for their detection on Mars. J. Volcanol. Geotherm. Res. 256, 61–77. https://doi.org/10.1016/j.jvolgeores.2013.02.009.
Craddock, R.A., Howard, A.D., 2002. The case for rainfall on a warm, wet early Mars. Journal of Geophysical Research: Planets 107 (E11). https://doi.org/10.1029/2001JE001505.
Dee, D.P., Uppala, S.M., Simmons, A.J., Berrisford, P., Poli, P., Kobayashi, S., Andrae, U., Balmaseda, M.A., Balsamo, G., Bauer, D.P., Bechtold, P., 2011. The ERA-Interim reanalysis: Configuration and performance of the data assimilation system. Q. J. R. Meteorol. Soc. 137 (656), 553–597. https://doi.org/10.1002/qj.828.
Deligne, N.I., 2012. After the Flow: Landscape Response to the Emplacement of Holocene Lava Flows, Central Oregon Cascades, USA. Ph.D. thesis. University of Oregon, Eugene, Oregon (217 p).
Dirscherl, M., Rossi, C., 2017. Geomorphometric analysis of the 2014–2015 Bárðarbunga volcanic eruption, Iceland. Remote Sens. Environ. 204, 244–259. https://doi.org/10.1016/j.rse.2017.10.027.
Dundas, C.M., Keszthelyi, L., Hamilton, C.W., Bonnefoy, L.E., Scheidt, S.P., Lev, E., Rumpf, M.E., Thordarson, T., Hoskuldsson, A., Jonsdottir, I., Keske, A.L., 2017. The hydrothermal system of the 2014–2015 lava flows at Holuhraun, Iceland: an analog for Martian lava–water interactions. Lunar and Planetary Science Conference. vol. 48 (Abstract 2470).
Dunne, T., 1980. Formation and controls of channel networks. Prog. Phys. Geogr. 4 (2), 211–239. https://doi.org/10.1177/030913338000400204.
Dunne, T., 1990. Hydrology, mechanics, and geomorphic implications of erosion by subsurface flow. Groundwater Geomorphology: The Role of Subsurface Water in Earth-Surface Processes and Landforms. vol. 252, pp. 1–28. https://doi.org/10.1130/SPE252-p1.
Eibl, E.P., Bean, C.J., Vogfjörd, K.S., Ying, Y., Lokmer, I., Möllhoff, M., O'Brien, G.S., Pálsson, F., 2017. Tremor-rich shallow dyke formation followed by silent magma flow at Bárðarbunga in Iceland. Nat. Geosci. 10 (4), 299–304. https://doi.org/10.1038/NGEO2906.
Ely, L.L., Brossy, C.C., House, P.K., Safran, E.B., O'Connor, J.E., Champion, D.E., Fenton, C.R., Bondre, N.R., Orem, C.A., Grant, G.E., Henry, C.D., 2012. Owyhee River intracanyon lava flows: does the river give a dam? GSA Bull. 124 (11—12), 1667–1687. https://doi.org/10.1130/B30574.1.
Feng, M., Whitford-Stark, J.L., 1986. The 1719–1721 eruptions of potassium-rich lavas at Wudalianchi, China. J. Volcanol. Geotherm. Res. 30 (1–2), 131–148. https://doi.org/10.1016/0377-0273(86)90070-3.
Fuller, E.R., Head, J.W., 2002. Amazonis Planitia: the role of geologically recent volcanism and sedimentation in the formation of the smoothest plains on Mars. Journal of Geophysical Research: Planets 107 (E10). https://doi.org/10.1029/2002JE001842.
Galeczka, I., Sigurdsson, G., Eiriksdottir, E.S., Oelkers, E.H., Gíslason, S.R., 2016. The chemical composition of rivers and snow affected by the 2014/2015 Bárðarbunga eruption, Iceland. J. Volcanol. Geotherm. Res. 316, 101–119. https://doi.org/10.1016/j.jvolgeores.2016.02.017.
Gíslason, S.R., Stefánsdóttir, G., Pfeffer, M.A., Barsotti, S., Jóhannsson, Th., Galeczka, I., Bali, E., Sigmarsson, O., Stefánsson, A., Keller, N.S., Sigurdsson, Á., Bergsson, B., Galle, B., Jacobo, V.C., Arellano, S., Aiuppa, A., Jónasdóttir, E.B., Eiríksdóttir, E.S., Jakobsson, S., Guðfinnsson, G.H., Halldórsson, S.A., Gunnarsson, H., Haddadi, B., Jónsdóttir, I., Thordarson, Th., Riishuus, M., Högnadóttir, Th., Dürig, T., Pedersen, G.B.M., Höskuldsson, Á., Gudmundsson, M.T., 2015. Environmental pressure from the 2014–15 eruption of Bárðarbunga volcano, Iceland. Geochemical Perspectives Letters 1 (1), 84–93. https://doi.org/10.7185/geochemlet.1509.
Goff, J.R., Ashmore, P., 1994. Gravel transport and morphological change in braided Sunwapta River, Alberta, Canada. Earth Surf. Process. Landf. 19 (3), 195–212. https://doi.org/10.1002/esp.3290190302.
Goldspiel, J.M., Squyres, S.W., 2000. Groundwater sapping and valley formation on Mars. Icarus 148 (1), 176–192. https://doi.org/10.1006/icar.2000.6465.
Graettinger, A.H., Ellis, M.K., Skilling, I.P., Reath, K., Ramsey, M.S., Lee, R.J., Hughes, C.G., McGarvie, D.W., 2013. Remote sensing and geologic mapping of glaciovolcanic deposits in the region surrounding Askja (Dyngjufjöll) volcano, Iceland. Int. J. Remote Sens. 34 (20), 7178–7198. https://doi.org/10.1080/01431161.2013.817716.
Gudmundsson, M.T., Jónsdóttir, K., Hooper, A., Holohan, E.P., Halldórsson, S.A., Ófeigsson, B.G., Cesca, S., Vogfjörd, K.S., Sigmundsson, F., Högnadóttir, T., Einarsson, P., 2016. Gradual caldera collapse at Bárdarbunga volcano, Iceland, regulated by lateral magma outflow. Science 353 (6296), aaf8988. https://doi.org/10.1126/science.aaf8988.
Gulick, V.C., 2001. Origin of the valley networks on Mars: a hydrological perspective. Geomorphology 37 (3–4), 241–268. https://doi.org/10.1016/S0169-555X(00)00086-6.
Gylfadóttir, S.S., 2016. Lágrennslisvísar. Greining þurrka og lágrennslistímabila í nokkrum vatnsföllum Landsvirkjunar. Icelandic Meteorological Office Report SSG/2016-01, Reykjavík.
Hamilton, C., 2015. Team gets firsthand look at the new Holuhraun eruption site. Eos 96. https://doi.org/10.1029/2015EO041197.
Harrison, K.P., Grimm, R.E., 2005. Groundwater-controlled valley networks and the decline of surface runoff on early Mars. Journal of Geophysical Research: Planets 110 (E12). https://doi.org/10.1029/2005JE002455.
Hartley, M.E., Thordarson, T., 2013. The 1874–1876 volcano-tectonic episode at Askja, North Iceland: Lateral flow revisited. Geochem. Geophys. Geosyst. 14 (7), 2286–2309. https://doi.org/10.1002/ggge.20151.
Hartley, M.E., Thordason, T., de Joux, A., 2016. Postglacial eruptive history of the Askja region, North Iceland. Bull. Volcanol. 78, 28. https://doi.org/10.1007/s00445-016-1022-7.
Higgins, C.G., 1982. Drainage systems developed by sapping on Earth and Mars. Geology 10 (3), 147–152. https://doi.org/10.1130/0091-7613(1982)10<147:DSDBSO>2.0.CO;2.
Hjartardóttir, Á.R., Einarsson, P., Gudmundsson, M.T., Högnadóttir, T., 2016. Fracture movements and graben subsidence during the 2014 Bárðarbunga dike intrusion in Iceland. J. Volcanol. Geotherm. Res. 310, 242–252. https://doi.org/10.1016/j.jvolgeores.2015.12.002.
Höskuldsson, A., Jónsdóttir, I., Thordarson, T., 2016. Futurevolc and the Bardarbunga eruption 2014–15 Iceland, success in the filed and laboratory. European Geosciences Union, General Assembly 18 (Abstract EGU2016-13687).
Howard, A.D., Moore, J.M., Irwin, R.P., 2005. An intense terminal epoch of widespread fluvial activity on early Mars: 1. Valley network incision and associated deposits. Journal of Geophysical Research: Planets 110 (E12). https://doi.org/10.1029/2005JE002459.
Howard, D.A., Luzzadder-Beach, S., Beach, T., 2012. Field evidence and hydraulic modeling of a large Holocene jökulhlaup at Jökulsá á Fjöllum channel, Iceland. Geomorphology 147–148, 73–85. https://doi.org/10.1016/j.geomorph.2011.07.031.
Huscroft, C.A., Ward, B.C., Barendregt, R.W., Jackson Jr., L.E., Opdyke, N.D., 2004. Pleistocene volcanic damming of Yukon River and the maximum age of the Reid Glaciation, west-central Yukon. Can. J. Earth Sci. 41 (2), 151–164. https://doi.org/10.1139/e03-098.
Ilyinskaya, E., Schmidt, A., Mather, T.A., Pope, F.D., Witham, C., Baxter, P., Jóhannsson, T., Pfeffer, M., Barsotti, S., Singh, A., Sanderson, P., Bergsson, B., Kilbride, B.M., Donovan, A., Peters, N., Oppenheimer, C., Edmonds, M., 2017. Understanding the environmental impacts of large fissure eruptions: aerosol and gas emissions from the 2014–2015 Holuhraun eruption (Iceland). Earth Planet. Sci. Lett. 472, 309–322. https://doi.org/10.1016/j.epsl.2017.05.025.
Jaeger, W.L., Keszthelyi, L.P., Skinner Jr., J.A., Milazzo, M.P., McEwen, A.S., Titus, T.N., Rosiek, M.R., Galuszka, D.M., Howington-Kraus, E., Kirk, R.L., 2010. Emplacement of the youngest flood lava on Mars: a short, turbulent story. Icarus 205 (1), 230–243. https://doi.org/10.1016/j.icarus.2009.09.011.
Jaenicke, J., Münzer, Ü., Minet, C., Eineder, M., Braun, L., Siegert, F., Gudmundsson, A., 2016. Volcanic activity at Bárðarbunga, Iceland, monitored with TerraSAR-X and Tan DEM-X data. TerraSAR-X/TanDEM-X Science Team Meeting, Oberpfaffenhofen, Germany, 17–20 October 2016.
Jefferson, A., Grant, G.E., Lewis, S.L., Lancaster, S.T., 2010. Coevolution of hydrology and topography on a basalt landscape in the Oregon Cascade Range, USA. Earth Surf. Process. Landf. 35 (7), 803–816. https://doi.org/10.1002/esp.1976.
Kiernan, K., Wood, C., Middleton, G., 2003. Aquifer structure and contamination risk in lava flows: insights from Iceland and Australia. Environ. Geol. 43 (7), 852–865. https://doi.org/10.1007/s00254-002-0707-8.
Kolzenburg, S., Jaenicke, J., Münzer, U., Dingwell, D.B., 2018. The effect of inflation on the morphology-derived rheological parameters of lava flows and its implications for interpreting remote sensing data – a case study on the 2014/2015 eruption at Holuhraun, Iceland. J. Volcanol. Geotherm. Res. 357, 200–212. https://doi.org/10.1016/j.jvolgeores.2018.04.024.
Lamb, M.P., Howard, A.D., Johnson, J., Whipple, K.X., Dietrich, W.E., Perron, J.T., 2006. Can springs cut canyons into rock? Journal of Geophysical Research: Planets 111 (E7). https://doi.org/10.1029/2005JE002663.
Lanagan, P.D., McEwen, A.S., Keszthelyi, L.P., Thordarson, T., 2001. Rootless cones on Mars indicating the presence of shallow equatorial ground ice in recent times. Geophys. Res. Lett. 28 (12), 2365–2367. https://doi.org/10.1029/2001GL012932.
Lowe, D.J., Green, J.D., 1987. Origins and development of the lakes. In: Viner, A.B. (Ed.), Inland Waters of New Zealand. DSIR Bulletin vol. 241. New Zealand Department of

Scientific and Industrial Research, Wellington , pp. 1–64. https://hdl.handle.net/10289/10555.

Luo, W., Howard, A.D., 2008. Computer simulation of the role of groundwater seepage in forming Martian valley networks. Journal of Geophysical Research: Planets (E5), 113 https://doi.org/10.1029/2007JE002981.

Maizels, J., 2002. 9- Sediments and landforms of modern proglacial terrestrial environments. Modern and Past Glacial Environments, pp. 279–316 https://doi.org/10.1016/B978-075064226-2/50012-X.

Mangold, N., Ansan, V., Masson, Ph., Quantin, C., Neukum, G., 2008. Geomorphic study of fluvial landforms on the northern Valles Marineris plateau, Mars. J. Geophys. Res. 113, E08009. https://doi.org/10.1029/2007JE002985.

Marra, W.A., McLelland, S.J., Parsons, D.R., Murphy, B.J., Hauber, E., Kleinhans, M.G., 2015. Groundwater seepage landscapes from distant and local sources in experiments and on Mars. Earth Surface Dynamics 3 (3), 389–408. https://doi.org/10.5194/esurf-3-389-2015.

Melosh, H.J., 2011. Planetary Surface Processes. vol. 13. Cambridge University Press, Cambridge, UK.

Mountney, N.P., Russell, A.J., 2004. Sedimentology of cold-climate aeolian sandsheet deposits in the Askja region of northeast Iceland. Sediment. Geol. 166 (3–4), 223–244. https://doi.org/10.1016/j.sedgeo.2003.12.007.

Münzer, Ü., Jaenicke, J., Eineder, M., Minet, C., Braun, L., Mayer, C., Siegert, F., Franke, J., 2016. Anwendung neuer Methoden mit hochauflösenden Fernerkundungs-daten (TerraSAR-X, TanDEM-X, RapidEye, UltraCam, HRSC) zur Früherkennung subglazialer Vulkanausbrüche auf Island. Final Report, pp. 1–85.

Nahm, A.L., Pendleton, M.W., Kattenhorn, S.A., 2016. Cerberus Fossae, Mars: the case for dike intrusion-related formation and modification. Acta Geol. Sin. 90 (1), 173–174. https://doi.org/10.1111/1755-6724.12957.

Pauly, K., 2016. Trimble UX5 HP–Increasing Your Productivity. White Paper. Trimble Navigation Limited 7pp. Available online at. uas.trimble.com/media/downloads.

Pedersen, G.B.M., Höskuldsson, A., Dürig, T., Thordarson, T., Jonsdottir, I., Riishuus, M.S., Óskarsson, B.V., Dumont, S., Magnússon, E., Gudmundsson, M.T., Sigmundsson, F., 2017. Lava field evolution and emplacement dynamics of the 2014–2015 basaltic fissure eruption at Holuhraun, Iceland. J. Volcanol. Geotherm. Res. 340, 155–169. https://doi.org/10.1016/j.jvolgeores.2017.02.027.

Pelletier, J.D., Baker, V.R., 2011. The role of weathering in the formation of bedrock valleys on Earth and Mars: a numerical modeling investigation. Journal of Geophysical Research: Planets 116 (E11). https://doi.org/10.1029/2011JE003821.

Pendleton, M.W., 2015. Geomorphic Evidence for Geologically Recent Groundwater Flow Associated with the Cerberus Fossae Magmatic and Volcanic System, Mars. MSc. Thesis, University of Idaho, 157 pp. ProQuest Dissertations Publishing. 1595198.

Reynolds, H.I., Gudmundsson, M.T., Högnadóttir, T., Magnússon, E., Pálsson, F., 2017. Subglacial volcanic activity above a lateral dyke path during the 2014–2015 Bárdarbunga-Holuhraun rifting episode, Iceland. Bull. Volcanol. 79 (6), 38. https://doi.org/10.1007/s00445-017-1122-z.

Richardson, J.A., Sutton, S., Whelley, P., Scheidt, S.P., Hamilton, C.W., Needham, D.H., Bleacher, J.E., 2018. Repeat field campaigns at Holuhraun, Iceland: exploring a new volcanic vent as a terrestrial analog for planetary surfaces. AGU Fall Meeting, 10–14 December 2018, Washington DC, USA, Abstract P51C-10.

Roach, I.C., Hill, S.M., Lewis, A.C., 2008. Evolution of a small intraplate basaltic lava field: Jerrabattgulla creek, upper shoalhaven river catchment, southeast New South Wales. Aust. J. Earth Sci. 55 (8), 1049–1061. https://doi.org/10.1080/08120090802266543.

Rossi, C., Minet, C., Fritz, T., Eineder, M., Balmer, R., 2016. Temporal monitoring of subglacial volcanoes with TanDEM-X–application to the 2014–2015 eruption within the Bárðarbunga volcanic system, Iceland. Remote Sensing of Environments 181, 186–197. https://doi.org/10.1016/j.rse.2016.04.003.

Ruch, J., Wang, T., Xu, W., Hensch, M., Jónsson, S., 2016. Oblique rift opening revealed by reoccurring magma injection in central Iceland. Nat. Commun. 7, 12352. https://doi.org/10.1038/ncomms12352.

Sara, M.J., 2017. Dyngjusandur Sandsheet, Iceland, as a Depositional Analog to the Stimson Fm. in Gale Crater, Mars. Doctoral dissertation. vol. 145. The University of Iowa.

Sara, M.J., Ukstins Peate, I., Riishuus, M.S., Yingst, R.A., Schmidt, M.E., Berger, J.A., Hartsock, T., 2017. Askja sandsheet, Iceland, as a depositional analog for the Stimson Fm. in Gale Crater, Mars. Lunar and Planetary Science Conference. vol. 48 (Abstract 2638).

Scheidt, S.P., Hamilton, C.W., 2019. Unmanned aerial system (UAS)-derived orthoimage mosaics and digital terrain models of the northeastern portion of the 2014–2015 Holuhraun lava flow-field, Iceland: Data acquired from 2015 to 2018. University of Arizona Spatial Data Explorer https://doi.org/10.2458/azu_geo_holuhraun_landscape_evolution.

Schorghofer, N., Jensen, B., Kudrolli, A., Rothman, D.H., 2004. Spontaneous channelization in permeable ground: theory, experiment, and observation. J. Fluid Mech. 503, 357–374. https://doi.org/10.1017/S0022112004007931.

Self, S., Keszthelyi, L., Thordarson, T., 1998. The importance of pāhoehoe. Annu. Rev. Earth Planet. Sci. 26 (1), 81–110. https://doi.org/10.1146/annurev.earth.26.1.81.

Sigmundsson, F., Hooper, A., Hreinsdóttir, S., Vogfjörd, K.S., Ófeigsson, B.G., Heimisson, E.R., Dumont, S., Parks, M., Spaans, K., Gudmundsson, G.B., Drouin, V., 2015. Segmented lateral dyke growth in a rifting event at Bárðarbunga volcanic system, Iceland. Nature 517 (7533), 191–195. https://doi.org/10.1038/nature14111.

Stearns, H.T., 1936. Origin of the large springs and their alcoves along the Snake River in southern Idaho. The Journal of Geology 44 (4), 429–450. https://doi.org/10.1086/624441.

Stearns, H.T., 1942. Hydrology of volcanic terranes. In: Meinzer, O.E. (Ed.), Hydrology. McGraw-Hill, Toronto, Ont, pp. 678–703.

Thordarson, T., Höskuldsson, Á., 2008. Postglacial volcanism in Iceland. Jökull 58, 197–228.

Thordarson, T., Self, S., 1993. The Laki (Skaftár fires) and Grímsvötn eruptions in 1783–1785. Bull. Volcanol. 55 (4), 233–263. https://doi.org/10.1007/BF00624353.

Thordarson, R., Larsen, G., Steinthorsson, S., Self, S., 2003. 1783–85AD Laki-Grimsvötn eruptions II: appraisal based on contemporary accounts. Jökull 51, 11–48.

Voigt, J.R.C., Hamilton, C.W., 2018. Investigating the volcanic versus aqueous origin of the surficial deposits in Eastern Elysium Planitia, Mars. Icarus 309, 389–410. https://doi.org/10.1016/j.icarus.2018.03.009.

Voigt, J., Hamilton, C.W., Scheidt, S.P., Bonnefoy, L.E., Jónsdóttir, I., Höskuldsson, A., Thordarson, T., 2017. Holuhraun 2014–2015 eruption site on Iceland: a flood lava analogue for Mars. European Planetary Science Congress. vol. 11 (Abstract EPSC2017-848-1).

Woodruff, J.F., Gergel, J., 1969. On the origin and headward extension of first-order channels. J. Geogr. 68 (2), 100–105. https://doi.org/10.1080/00221346908981067.